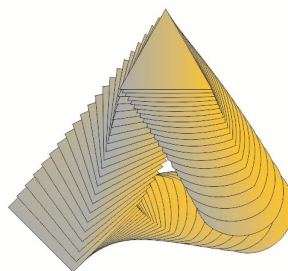


**Eighth International Conference on
Local Mechanical Properties LMP 2011**

Olomouc, Czech Republic

9–11 November 2011

***LOCAL
MECHANICAL
PROPERTIES
2011***



Organized by

**Joint Laboratory of Optics
Palacky University and Institute of Physics
Academy of Sciences of the Czech Republic**

2011

s367

SPONSORS OF THE CONFERENCE



Preface

The Eighth International Conference on Local Mechanical Properties LMP 2011 was held in Olomouc, The Czech Republic, on November 9-11, 2011. The LMP 2011 conference was organized by the Joint Laboratory of Optics of Palacky University and Institute of Physics of the Academy of Sciences of the Czech Republic.

Continuing in the tradition of the LMV (Lokální mechanické vlastnosti) conference series started in 2004, the LMP 2011 brought together material specialists, researchers and scientists from universities, research institutes and also the private companies representatives. It was again a really open forum for the intensive discussion and exchange of knowledge and experience.

The meeting that becomes a well established forum in the field of local mechanical testing provided an opportunity to highlight recent results of research and development in the field of materials engineering, experimental methods, modeling, etc., with the aim to characterize mechanical properties of broad range of materials from nano to micro/meso-scale. Especially nanoindentation and other methods of hardness assessment, measurement of local stresses and deformations and related microstructure analyses were discussed.

Over 90 participants from 11 countries around the world attended this conference. The conference program covered 35 oral presentations in 8 sections and 53 posters on recent progress in research, development and applications of measurement of mechanical properties at small scale.

The LMP 2011 conference organizers would like to thank all the speakers, session chairpersons, invited speakers and participants for making this conference successful. The support of the conference sponsors is also greatly appreciated. It is our hope that LMP 2011 conference has been fruitful and presented works will provide valuable information and guidance on the latest trends and future advances in local mechanical testing. This issue contains 68 peer reviewed papers.

EDITORS

Dr. Radim Čtvrtlík (UP Olomouc)
Prof. Ladislav Pešek (TU Košice)

CHAIRS OF THE CONFERENCE

Dr. Radim Čtvrtlík (UP Olomouc)
Prof. Ladislav Pešek (TU Košice)
Assoc. Prof. Olga Bláhová (ZČU Plzeň)

LOCAL ORGANIZING COMMITTEE

Dr. Radim Čtvrtlík
Dr. Petr Hamal
Dr. Hana Lapšanská
Dr. Dušan Mandát
Daniela Nantlová
Dr. Libor Nožka
Dr. Miroslav Pech
Dr. Pavol Zubko

SCIENTIFIC BOARD

Dr. Robert Bidulský
Assoc. Prof. Olga Bláhová
Dr. Radim Čtvrtlík
Dr. Małgorzata Garbiak
Dr. Pavol Hvizdoš
Assoc. Prof. František Lofaj
Prof. Jaroslav Menčík
Assoc. Prof. Jiří Němeček
Prof. Ladislav Pešek
Dr. Ulrich Prah
Assoc. Prof. Galina Zamfirova
Dr. Pavol Zubko

Declaration

All contributions included in the special issue of this journal have been reviewed prior to publication by the members of the Scientific Board. Linguistic usage in the articles has not been modified by the editors.

CELLS ON SURFACES: AN INDENTATION APPROACH

MICHAEL V. SWAIN^{a,b}, S. SCHULZ^a,
T. STEINBERG^a, and P. TOMAKIDI^a

^a Department of Prosthodontics, School of Dentistry, Albert-Ludwigs University, Freiburg, Germany,

^b Biomaterials, Faculties of Dentistry, The University of Sydney, Australia and Otago University, Dunedin, New Zealand

michael.swain@uniklinik-freiburg.de

Keywords: cells, surface interaction, pillars, indentation

1. Introduction

Recent studies have established the critical role for cells of the mechanical properties of the extra-cellular matrix on which they are supported. It has been shown that mesenchyme stem cells can differentiate into specific cells ranging from nerve to bone. In addition it is known that cells in attachment with a substrate generate traction forces which contribute to their movement and reorientation.

The mechanical properties, dimensions and structural form of the filamentous components of cells are also well investigated. In addition, the basic cell membrane properties have been investigated by many authors using a variety of techniques including; micro pipette, optical tweezers, shear flow and magnetic particle interaction and nano-indentation being the most common¹. The basis for interpretation of the force-displacement data is very different from the analysis of indentation of elastic-plastic materials.

Various techniques based upon those developed for semiconductor production to develop surfaces that enable the micromechanical responses of cells to be explored. Micro-grooving, dimples and micro-pillars enable a number of variables of surfaces to be investigated in a systematic manner. For pillars these include the roles of elastic modulus, height, spacing and diameter as a means to influence cell response. The majority of these studies focussed on the role of the surface on the subsequent cell morphology along with incorporation of various fluorescent dyes to enable the various filament structures to be visualised.

A critical review of this area by Flemming et al.² identified the effect of features, primarily that of micro grooving and the resulting cell morphology and growth. They noted that cells tended to align parallel to grooves and the cytoskeleton components formed parallel to the grooves. The work of Wojciak-Stothard et al.³ noted that actin filament condensation appeared at topographic discontinuities. Flemming et al.² indicated the depth of grooves were more important than width in determining

cell orientation. More recently Martinez et al.⁴ used cryo and subsequent focussed ion beam (FIB) sectioning to investigate the role of pattern spacing and height on the basal response of cells to surfaces. They observed with line patterns that it was the ratio of pattern height to width that was critical.

Recent work has placed considerable focus on biochemical, gene expression responses and the traction forces developed on various surfaces. Again the feature that is persistently remarked upon in these studies is the location of the various cells investigated as a function of pillar height, diameter and spacing. At relatively close pillar spacing the cells sit on top of the pillar arrays whereas at larger pillar spacing they lie between the pillars.

Steinberg et al.⁵ investigated PDMS pillars with E moduli of 0.5 to 3.5 MPa and 8 to 14 μm spacing on keratinocyte cell differentiation. They observed that with a decrease in pillar spacing an increase in the cell differentiation. Mussig et al.^{6,7} investigated 3 periodontal type cells on cell morphology and gene expression. Pillar spacing of 5 μm enabled regular cellular response for all cells, increasing pillar spacing resulted in reduced cell numbers. Cell observations with the osteoblasts indicated the cells were only slightly indented when pillars were 5 μm apart but more substantially indented and almost resting on the space between the pillars at 11 μm spacing. A recent study by Papenberg et al.⁸ investigated wettability of micro-pillars of three materials (PDMS, PEOT/PBT and PLLA) with E modulus (2 MPa, 30–70 MPa to 2 GPa) with pre-myoblasts cells. For pillar spacing of 2 μm all cells grew on top of the pillars while at 5 μm spacing there was a transition from growing on top of the pillars to between the pillars especially for the 5 μm high pillars. The authors state surface topography rather than pillar elastic modulus influenced cell attachment, proliferation and morphology.

The aim of the present paper is to more closely investigate the interaction mechanics between various cells and the micro pillars they are supported on. A simple generalised contact analysis of the cell pillar interaction is developed that is used to compare with the experimental observations. The simple contact mechanics and cell membrane deformation concepts are then applied to a number of cell systems published in the literature

2. Materials and methods

As stated above, many authors have used micro pillars to support cells in order to study the morphological, detailed microbiological and gene expression responses. These pillars are generally fabricated using photolithography based procedures with tailored diameter, pillar height and spacing. Details regarding the development of such

materials are given in the studies by Steinberg et al.⁵. A typical SEM observation of such pillars is shown in Fig. 1.

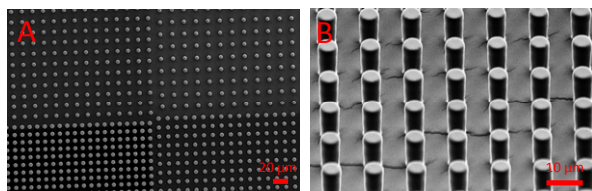


Fig. 1. SEM images of a PDMS pillar array with pillar heights of 15 μm, pillar diameters of 5 μm and spacing between the pillars varying between 5 to 11 μm. Note that four pillar spacing distances have been created simultaneously. A normal and B inclined view

Various approaches have been used to visualise cells including confocal and optical microscopy, SEM as well as an array of staining and visualisation approaches. SEM often results in dehydration induced shrinkage of the cells during preparation. In this study details of micro-biology or gene expression outcomes will not be addressed directly.

3. Contact and deformation mechanics

In this section only the initial phase of cell deformation that is, the contact pressure between the pillars and the cell membrane is considered.

3.1. Contact mechanics

Consider a cell as a spherical entity with a plasma membrane having a constant volume, V , and density, ρ . It is suspended in a fluid culture medium that has a density of $\rho_0 \sim 1$ gm/cc. When the cell rests on the pillars then contact stresses are developed between the pillar and cell membrane. Consider a square array of cylindrical pillars with diameter D that have a centre to centre spacing of L , Fig. 2.

Consider the cell upon contacting the pillars to form into a hemispherical shaped body then the relationship

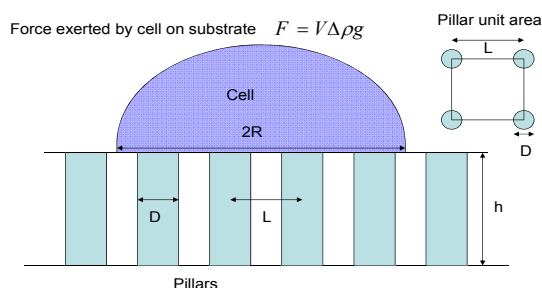


Fig. 2. Schematic illustration of a cell on an array of pillars with dimensions and spacing defined

between the volume, V , of the cell and its radius, R , is:

$$V = \frac{2}{3} \pi R^3 \quad (1)$$

The support area of an individual pillar is given by $A_p = \pi D^2/4$. For a square array of pillars with spacing L between the pillar centres, each pillar contributes one quarter to the unit cell area of the pillar array, and is given by, Pillar area per unit cell

$$= \frac{\pi D^2}{4L^2} \quad (2)$$

For a cell of volume V that forms into a hemispherical body upon contact with the array, the diameter of the cell is $2R$ (Fig. 3). The contact area assuming the pillar array a continuous flat surface is given by πR^2 . Thus the supporting area provided by the pillars beneath the cell is given with eq (2) by,

$$A_p = \left(\frac{\pi D^2}{4L^2} \right) (\pi R^2) = \left(\frac{\pi DR}{2L} \right)^2 \quad (3)$$

The force exerted by the cell on the supporting contact area in the liquid media is given by;

$$F = V \Delta \rho g \quad (4)$$

where V is the cell volume, $\Delta \rho$, that is $(\rho - \rho_0)$ is the density difference between the cell and supporting liquid medium and g is the gravitation constant. The average contact pressure between the cell and the pillars is then given from eqs (3) and (4), namely;

$$P_c = \frac{F}{A_p} = \frac{V \Delta \rho g}{(\pi DR / 2L)^2} = \frac{8RL^2 \Delta \rho g}{3\pi D^2} \quad (5)$$

Contact pressure on cell membrane by each pillar. $P_c = \frac{F}{A_p} = \frac{V \Delta \rho g}{(\pi DR / 2L)^2} = \frac{2\pi R^3 \Delta \rho g}{3(\pi DR / 2L)^2} = \frac{8RL^2 \Delta \rho g}{3\pi D^2}$

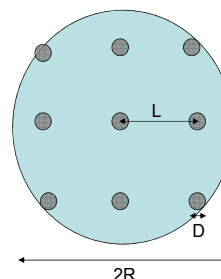


Fig. 3. Schematic diagram of projected cell supported on an array of pillars

For a specific cell with similar volume and for pillars of constant diameter the contact pressure is directly related to L^2 . For the pillar spacings considered there is almost a 4 fold increase in the contact pressure as L changes from 10 to 19 μm . The relationship between centre to centre pillar spacing L with diameter D and often stated edge to edge spacing X is $L = D + X$.

Fig. 4 is plotted, from eq (5), the dependence of the contact pressure as a function of pillar spacing L pillar diameter D for cell where $\Delta\rho$ is 0.3 kg m^{-3} .

3.2. Stresses and axial deflection of pillars

The force on the pillar due to the loading by the cell is given by

$$F_p = \frac{V\Delta\rho g}{n} \quad (6)$$

where n is the number of pillars supporting the cell, which is given by the ratio of the area of the cell divided by the pillar array unit cell area, namely;

$$n = \frac{\pi R^2}{L^2} \quad (7)$$

Substituting into eq (7) for n and V from eq (1), results in

$$F_p = \frac{2\Delta\rho g R L^2}{3} \quad (8)$$

The resultant axial compressive stress on the pillars is then given by the pillar force divided the cross sectional area of the pillar, namely

$$\sigma_p = \frac{8\Delta\rho g R L^2}{3\pi D^2} \quad (9)$$

and the resultant displacement, ζ_p , of a pillar of height, h , and elastic modulus, E , due to this stress is given by

$$\zeta_p = \frac{8\Delta\rho g R L^2 h}{3\pi D^2 E} \quad (10)$$

The maximum displacement experienced by a pillar for a value of L of 20 μm , R of 25 μm , h of 15 μm , D of 5 μm on a PDMS pillar of 0.6 MPa E modulus is only $\sim 25 \text{ pm}$. That is axial displacement or deformation of the pillars by cells on even the softest pillars is negligible. For line contact the stresses and deflections would be even lower.

4. Results

4.1. SEM and Optical images

Typical SEM image of successfully achieved keratinocyte adhesion and viability on the micro-pillar

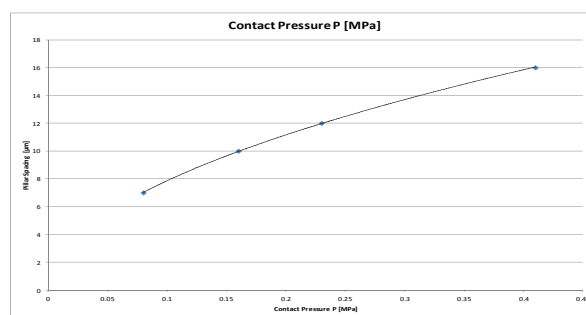


Fig. 4. Contact pressure (from Eq (5)) between pillar and cell as a function of pillar spacing, L . Pillar diameter 5 μm and cell radius R of 15 μm

interfaces, the interpillar distances are shown in Fig. 5. While keratinocytes, cultured on FN coated pillars with interpillar distances of 8 μm and 5 μm (the later shown in Fig. 5a), covered the pillar tops and were quite round-shaped, the cells clearly penetrated into the micropillar field on substrates with distances of 11 μm and greater (Fig. 5b).

The shape of the latter cells had a more linear or triangular shape depending on how many pillars they covered. To exclude drying artefacts from the sample preparation for the electron microscopy and to ensure successful adhesion of the keratinocytes, they were stained by IIF for the focal adhesion kinase (FAK), see Steinberg et al.⁵ paper for typical images. The results obtained optically confirmed the morphological differences observed in the SEM.

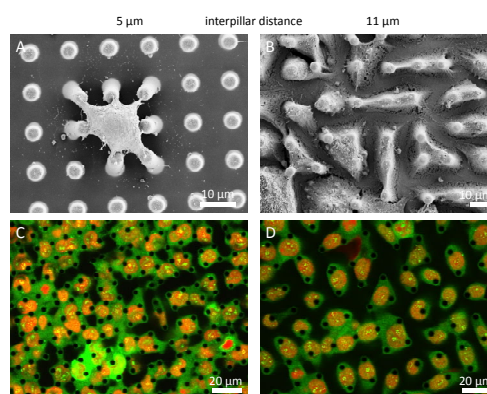


Fig. 5. Morphology differences of keratinocyte on pillar fields with pillar spacing of 5 μm (A, C) and 11 μm (B, D): SEM of (A) a keratinocyte spread on a FN-coated pillar field. The cell adheres to the pillar top while in (B) it sinks into the substrate. Fluorescent images of the cells stained for FAK (green) ((C), (D)) reveal the same morphological differences

4.2. Confocal images

Typical examples are shown in Fig. 6a and 6b. On the substrate with pillar spacing of 5 μm the keratinocytes were round shaped, covered pillar tops (Fig. 6a) and penetrated slightly into the micro-pillar field. The FAK was stained green with a counter stain of the cell nuclei in red. 3D reconstructions enabled visualisation of the pillar protrusion into the cells.

A different morphology was observed for cells cultured on substrates with pillar spacing of 11 μm (Fig. 6b). The cells were more linear shaped and penetrated almost completely into the micropillar field. The 3D images confirmed the extent of penetration of the pillars into the cells. A more extensive study showed that keratinocyte differentiation varies with respect to different interpillar distances.

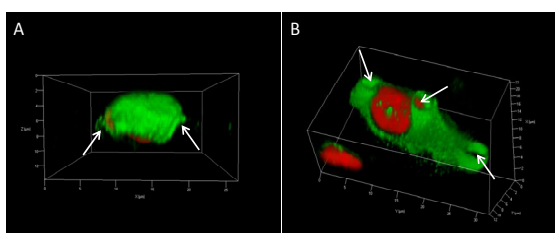


Fig. 6. Confocal images of cells sitting on pillars spaced A) 5 μm and B) 11 μm apart. Arrows point to where pillars were acting on the cells. The green fluorescence arises from focal adhesion kinase (FAK) while the red stain shows the cell nuclei

4.3. Indentation depth

Confocal images (Fig. 6) indicate that the depth of penetration of the keratinocyte cells when the pillar spacing 5 μm apart is only 1 to 2 μm whereas for the 11 μm spacing the pillars protruded the entire height.

5. Discussion

The observations shown in Fig. 6 indicate that contact stresses generated by the pillars on the keratinocyte cell membrane under the gravitational force acting on the cells in the culture medium are sufficient to cause significant deformation of the membrane. These observations are similar to those by Mussig et al.^{6,7} for osteoblast cells. Considering the observed indentation protrusion of the pillars into the cells as shown in Fig. 6 there is a clear influence of pillar spacing and as such contact pressure between the membrane and the pillars. From the analysis above the contact pressure for the two conditions shown in Fig. 6, namely eq (5), can be estimated. In the case of the edge spacings shown (5 and 11 μm) the values of L in eq (5) are $X + D$, namely 10 and 16 μm respectively. The calculated mean contact pressures between the pillars and these keratinocyte cells are 0.16 and 0.41 MPa respectively with the radius of the keratinocyte cell as 15 μm . The confocal observations suggest that the protrusion depth

does not scale linearly with the contact pressure as a 2.5 fold increase in contact pressure changes the depth of protrusion of the pillars into the cells by greater than a factor of 5. These conclusions are in agreement with the response of Mussig et al.^{6,7} and also Papenberg et al.⁸ who considered different cell types. The latter study also considered pillars of different elastic rigidity and changed the wettability of the pillars and minimal change was observed in terms of the cell deformation by the pillars. The simple analysis above also indicates that for the range of pillar materials considered by Papenberg et al.⁸ the extent of axial displacement of the pillars by the cells is negligible. There would be greater horizontal deflection of the softer material for the longer pillars as a consequence of the actin myosin motor development. Direct nano-indentation studies of various shaped indenters into cells by Evans et al.⁹ and Hartegan et al.¹⁰ indicate very extensive cell membrane deflection of many μm s at nN forces. However a major difference between the present observations and those of direct nano-indentation testing of cells is the time scale of the experiments. In the nanoindentation tests typically a minute or two is the test duration whereas the current observations were made after 24 hours contact between the cells and pillars. This time difference for the two approaches raises two important issues namely the role of visco-elastic response of the cell membrane under stress and also the response of the cytoskeleton machinery within the cell. Here the former will not be discussed but rather more a focus placed upon the latter effects.

At the contact sites between cells and pillars the local stress initiates actin filament nucleation and growth. The stress state in the membrane about the pillars is complex but the areas of highest tensile stress are at the boundaries that become more uniform between the pillars. The rate of filament growth is relatively rapid and dependent upon the stress level. According to Fletcher and Mullins¹¹ the form of the network of actin filaments is highly dependent upon the stress. Considering first the top of the pillars, this would experience compression and result in assemblage into a type a mesh structure. Whereas at the edge of the pillars tensile stresses develop, resulting in a more randomised type of mesh formation. In both instances as well continuous filament formation nucleation sites develop on these for growth of cross hatching filaments. Such 3D meshes provide additional rigidity of the cell against local stress and penetration of the pillars. These mesh structures will continue to grow depending upon the extent of the actin precursor concentration in the cell.

In addition the observations in Fig. 6 show that focal adhesion kinase (FAK), which is an indicator of intermediate filament development, has also occurred and is concentrated at the base of the cells and appears to act to support the cell membrane. It would also be expected that the microtubular filaments within the cell, which are of more radial formation, would also respond to the stresses imposed on the cell by the pillars. In addition there are linkages between the three filamentous structures that could further enhance the effective rigidity of the cell. However

as all these filamentous components are essentially polymers they take time to grow and hence the associated effective rigidity of the cell membrane takes time. For the confocal observations shown above it appears that for the closely placed pillars there has been sufficient time for the cytoskeleton machinery to respond and reinforce the membrane rigidity thereby limiting the extent of pillar protrusion into the membrane. Whereas for the 11 μm spaced pillars there is a comparable development of the FAK and presumably other filamentous structure, but not before the pillars have extensively protruded into the cells.

REFERENCES

1. Bao G. & Suresh S.: *Nature Mat.* 2, 715 (2003).
2. Flemming R. G., et al.: *Biomater.* 20, 573 (1999).
3. Wojciak-Stothard B., et al.: *Exp. Cell Res.* 223, 426 (1996).
4. Martinez E., et al.: *Micron* 39, 111 (2008).
5. Steinberg T., et al.: *Nano Lett.* 7, 287 (2007).
6. Mussig E., et al.: *Eur. J. Cell Biol.* 89, 315 (2010).
7. Mussig E., et al.: *Adv. Funct. Mat.* 18, 2919 (2008).
8. Papenberg B., et al.: *Soft Mater.* 6, 4377 (2010).
9. Evans E.: *Biophys. J.* 68, 2580 (1995).
10. Hategan A., et al.: *Biophys. J.* 85, 2746 (2003).
11. Fletcher D. A., Mullins R. D.: *Nature* 463(7280), 485 (2010).

M. V. Swain^{a,b}, S. Schulz^a, T. Steinberg^a, and P. Tomakidi^a (^a *Department of Prosthodontics, School of Dentistry, Albert-Ludwigs University, Freiburg, Germany,* ^b *Biomaterials, Faculties of Dentistry, The University of Sydney, Australia and Otago University, Dunedin, New Zealand*): **Cells on Surfaces: an Indentation Approach**

A simple contact mechanics approach is developed to investigate the initial response of biological cells resting on patterned pillar surfaces. The results are compared with recent cell morphology observations by a number of groups. It is evident that the changing internal cytoskeleton of the cell and its time dependence plays an important role in determining the developing cell morphology.

GEOMETRICAL AND MICROHARDNESS ASPECTS OF ALUMINIUM PM ALLOYS AS FUNCTION OF LOCAL PLASTIC DEFORMATION

RÓBERT BIDULSKÝ^a, JANA BIDULSKÁ^b,
and MARCO ACTIS GRANDE^a

^a Politecnico di Torino, Department of Applied Science and Technology, 15121, Alessandria, Italy, ^b TU of Kosice, Faculty of Metallurgy, Dpt. of Metals Forming, 042 00, Košice, Slovakia
robert.bidulsky@polito.it, marco.actis@polito.it, jana.bidulska@tuke.sk

Keywords: aluminium alloys, compaction, compressibility, porosity, microhardness, FEM

1. Introduction

In terms of cost effectivity, the traditional uniaxial powder consolidation process is still widely employed for the production of powder metallurgy (PM) parts, especially for the automotive industry. PM is a well established technology for manufacturing parts to net or near net shape and in the present time, the growing demand for weight reductions in automotive applications has pushed the PM industry to develop components on the basis of light material^{1–3}.

2. Material and experimental conditions

Commercial ready-to-press aluminium based powders, ECKA Alumix 321 (Al-0.95Mg-0.49Si-0.21Cu-0.07Fe-1.5lub) and ECKA Alumix 431 (Al-5.8Zn-2.6Mg-1.7Cu-0.23Sn-1.5lub), were used as materials to be investigated. Particles size distribution was carried out by sieve analyzer according to ISO 4497. Test specimens 55×10×10 mm³ were uniaxially pressed in a hardened floating steel die. The green compacts were weighed with an accuracy of ±0.001 g. The dimensions were measured with a micrometer calliper (±0.01 mm). Microhardness was recorded by Duramin-5 Tester on minimum 15 points. For the identification of the compressibility behaviour different compacting pressures were applied (50, 100, 200, 300, 400, 500, 600 and 700 MPa) and the following compressi-

$$P = P_0 \cdot \exp(-K \cdot p^n), [\%] \quad (1)$$

bility equation⁴ was used:

Where: P – porosity achieved at an applied pressure p , [%]; p – applied pressure, [MPa]; K – parameter related to particle morphology, [-]; n – parameter related to activity of powders to densification by the plastic deformation, [-]; P_0 – apparent porosity calculated from the value of experi-

$$P_0 = \left[1 - \frac{\rho_a}{\rho_{th}} \cdot 100 \right], [\%] \quad (2)$$

mentally estimated apparent density, [%]:

where: ρ_a – apparent density, [g cm⁻³]; ρ_{th} – theoretical density, [g cm⁻³].

3. Results and discussion

Tab. I shows data for the calculated compressibility parameters K , n and correlation coefficient r . According to data listed in Tab. I, the compressibility parameter n is related to activity of powders to densification by the plastic deformation. In case of powders with high plasticity, n is close to 0.5; in case of low plasticity, n is close to 1. System A ($n = 0.5175$) shows a higher ability to plastically deform than system B ($n = 0.6181$).

The effect of powder morphology is reflected in the values of compressibility parameter K , which is lower for powder B ($K = 0.479 \cdot 10^{-2}$) than for powder A ($K = 1.161 \cdot 10^{-2}$). The difference between powder A and B is connected with the effect of particle geometry. Particle geometry is linked to the morphological properties as well as particle size distribution (A: $d_{50}=100 \mu\text{m}$, B: $d_{50}=63 \mu\text{m}$). Morphological aspect of powder shape is controlled by manufacturing process. Tab. I shows that the fitting experimental data and calculated data are higher than 0.96 (last column). The compressibility equations for the studied systems are reported as follows:

Table I

Theoretical density values, apparent porosity, compressibility parameters and correlation parameters

No.	ρ_{th} [g.cm ⁻³]	P_0 [%]	K [-]	n [-]	r [-]
A	2.6229	58.44	$1.161 \cdot 10^{-2}$	0.5175	0.9675
B	2.7213	59.58	$0.479 \cdot 10^{-2}$	0.6181	0.9899

$$\text{A: } P = 58.44 \cdot \exp\left(-0.1161 \cdot p^{0.5175}\right) \quad (3)$$

$$\text{B: } P = 59.58 \cdot \exp\left(-0.0479 \cdot p^{0.6181}\right) \quad (4)$$

Table II
Microhardness values of studied PM aluminium alloys at various pressing pressures

No. / p [MPa]	50	100	200	400	500	600	700
A	17.8±4.2	21.4±4.3	25.4±5.9	29.4±4.2	32.2±2.6	34.6±3.5	35±3.6
B	19.3±3.0	24.8±2.9	31.9±5.1	33.3±2.3	36.3±2.5	40.6±5.7	39.2±4.7

Geometrical rearrangement plays an important role during the densification process (as well as plastic deformation). Moreover, also the compressibility parameter K has to be considered as an indicator of the physical-metallurgical characteristics including the geometrical and morphological characteristics of metal powder particles. Authors^{4,5} underline that parameter K depends, mainly, on the microhardness values, Tab. II. Microhardness (strongly impacted by yield stresses) as well strengthening coefficient represents essential parameters of metal powder plasticity.

Tab. II shows that microhardness values increase with increasing pressing pressure. At higher pressing pressure, 600 MPa, previous investigations^{1,3} show that the final stages of densification of powder particles are achieved. Therefore, the higher applied pressure at 700 MPa shows lower microhardness value due to the spring back effect as results of work hardening and exhaustion of plasticity in some local volume and relaxation.

During PM production, the employed compaction conditions dictate the stress and density distribution in the green compact prior to sintering, these parameters having a profound influence on the overall strength of the final component. The distribution of stress and strain during pressing can be predicted by means of finite element method (FEM). FEM analysis helps understanding the complexity of stress-strain processes^{6,7}. Compressibility parameters K and n cover the plastic deformation processes performed during pressing as well as those defined by the physical significance. Moreover, they enable to quantify the intensity of the development of compaction facets. The dimensions of particle contact areas depend primarily on particle shape and the localization of plastic deformation depends on surface geometry and pressure level. This means that the compaction facets, as results of overall compressibility effect, depend on granulometry, compaction pressure, and particle surface roughness form discontinuous adhesive and mechanical particle contacts.

4. Conclusion

The results show that the development of compressibility values with pressing pressure enables to characterize the effect of particles geometry and matrix plasticity on the

processes performed during pressing. The compressibility results exhibit a high value of plasticity, as a property related to compressibility parameters K and n .

R. Bidulský thanks the Politecnico di Torino, the Regione Piemonte, and the CRT Foundation for co-funding the fellowship. J. Bidulská thanks Slovak national project VEGA 1/0385/11.

REFERENCES

- Bidulská J. et al.: Chem. Listy 105, s471 (2011).
- Lefebvre L.P., Thomas Y., White B.: J. Light Met. 2, 239 (2002).
- Kvačkaj T., Bidulský R. (ed.): *Aluminium Alloys, Theory and Applications*. InTech, Rijeka 2011.
- Dudrová E. et al.: *Powder Metallurgy in ČSSR*, Part 1, p. 73. Brno, Žilina: DT ČSVTS, 1982 (Lecture).
- Šlesár M. et al.: *Pokroky Praskove Metal. VUPM 18*, 3 (1980).
- Kvačkaj T. et al.: *Kovove Mater.* 45, 249 (2007).
- Kvačkaj M., Kvačkaj T., Kováčová A., Kočíško R., Bacsó J.: *Acta Metall. Slovaca* 16, 84 (2010).

R. Bidulský^a, J. Bidulská^b and M. Actis Grande^a
(^a Politecnico di Torino, Department of Applied Science and Technology, Alessandria, Italy, ^bTU of Kosice, Faculty of Metallurgy, Dpt. of Metals Forming, Slovakia): **Geometrical and Microhardness Aspects of Aluminium PM Alloys as Function of Local Plastic Deformation**

The paper deals with the compressibility analysis of PM aluminium alloys Al-Mg-Si-Cu-Fe and Al-Zn-Mg-Cu-Sn. Compaction pressures ranged from 50 MPa up to 700 MPa. Considering the densification of metal powders in uniaxial compaction, quantification of aluminium compaction behaviour was performed using the linear regression analysis. The compressibility behaviour was evaluated in relation to geometry and mechanical properties of powder particles on pressing pressure as well as microhardness values. The development of compressibility values with pressing pressure enables to characterize the effect of particles geometry and matrix plasticity on the compaction process.

NUMERICAL MODELLING OF THE NANOCOMPOSITES IN STEEL/Ti-B-C SYSTEM

ANNA BIEDUNKIEWICZ, WITOLD BIEDUNKIEWICZ, PAWEŁ FIGIEL, and DARIUSZ GRZESIAK

*West Pomeranian University of Technology Szczecin,
Piastow Ave. 17; 70-310 Szczecin, Poland
Anna.Biedunkiewicz@zut.edu.pl*

Keywords: nanocomposite, FEM, SLS/M, 316L steel, TiC, TiB₂, B₄C

1. Introduction

Metal matrix composites (MMCs) are the focus of intense research and development world wide for many industrial branches. B₄C ceramics have some excellent physical and chemical properties. Its ultrahigh hardness, high wear and impact resistance, low specific weight and good chemical stability makes it suitable for application in ball mills, blasting nozzles, wheel dressing tools, wire drawing dies, rocket propellant light weight armour plates and mechanical seal faces, etc^{1,2}. TiB₂ and TiC have attracted great interest in their excellent mechanical properties, chemical resistance and good thermal and electrical conductivities. The composites containing the TiC and TiB₂ phases are characterized by good fracture and wear resistance and the increase in their hardness along with the increase in temperature^{4,5}.

Our work presents the comparison of the results of investigations on 316L steel and nanocomposites manufactured by SLS/M method. The differences in mechanical properties between steel, 316L steel/TiC and 316L steel/Ti-B-C composites based on the results of modelling by numerical method are presented.

2. Experimental details and results

The technology of the production of nanocomposite structures based on the Selective Laser Sintering/Melting technology has been worked out⁶⁻⁸. The stainless steel 316L was used as a matrix and as the filler nc-TiC and nc-Ti-B-C powders were used. Before the SLS/M the powders were prepared by ball-milling method. In the SLS/M process the following parameters were used: the laser power: 5000 mA; the exposure time: 200 μs, s layer thickness: 50 μm. Samples were subjected to hardness tests for quick estimation of the mechanical parameters. Hardness and modulus measurements were performed on MTS Nano Indenter XP using Brekovich tip (Tab. I).

Table I
Hardness (H) and elastic modulus (E) values of the samples

	H [GPa]	E [GPa]
Steel 316L	4,77	201
60% vol TiC	9,93	230
20% vol Ti-B-C	17,75	263

2.1. FEM model

For prediction of the result of introducing additional phases into the composite, two-variant FEM model of the structure has been prepared. The Representative Volume Element (RVE) with dimensions 1×0.5×0.5 μm (X,Y,Z) has been taken instead of the bulk structure for making calculation time reasonable. The amount of all three filler phases was equal and together it came up to 15% of whole volume. The rest of the volume was the steel matrix. The fillers particles were mixed and randomly distributed in the whole RVE.

Material models of the filler particles were taken as perfectly elastic with the following parameters: TiC: E = 460 GPa, d = 4800 kg m⁻³; TiB₂: E = 560 GPa, d = 4500 kg m⁻³; B₄C: E = 660 GPa, d = 2520 kg m⁻³. The matrix was modeled as elastic-plastic material with the following parameters: E = 193 GPa, d = 8000 kg m⁻³, yield stress = 250 MPa.

To simulate the bulk structure, periodic boundary was applied to the whole RVE and to estimate the mechanical properties of composites, simulation of the tension was used in which uniaxial monotonic displacement in X direction was applied to the opposite sides of the RVE. Value of the displacement was increased up to the value of 2% of the RVE size and then decreased to the value of zero.

The structure was meshed with C3D4 elements (a 4-node linear tetrahedron). To avoid any mesh changes, there were no remeshing rules used. After all preparing operations were finished and before the calculation stage, the model was copied and in the newly created version only the material parameters of B₄C and TiB₂ phases were replaced with the values equal to the TiC. Such prepared models were identical in every case (including geometrical shape of the mesh), except of the material properties of the particles representing filler phase of the composite. Additionally the model made of pure steel was prepared with the same technique to compare it to both composites types. As comprised parameter the reaction force measured in reference point in which the tension was applied was taken. The resulting plots of force courses for all three models are presented in Fig. 1.

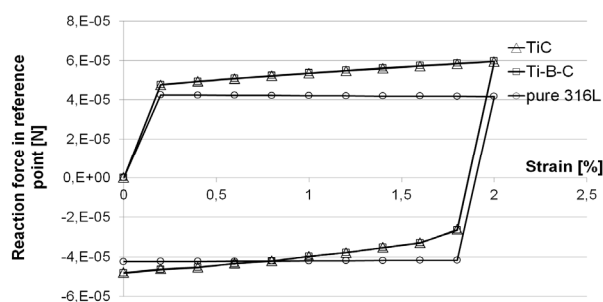


Fig. 1. Values of the reaction forces during the load and un-load of the samples

In the Fig. 2 the result of the subtraction of the forces values obtained from the steel/TiC composites from the forces values obtained from the steel/(TiC+TiB₂+B₄C) composite are presented.

As can be seen, the differences between both composites are very small and the significant difference is observed in the case of pure steel. Because of using periodic boundary conditions, the resulted values representing mechanical properties of the pure steel model are equal in whole RVE, which proves ideal representation of bulk structure. In the case of composite, inclusions are generating variable values of the same parameter (plastic strain for example), which apparently can cause the composite stiffness increase and because of big amount of small particles in nanocomposites, it can be one of the reasons of superhardness effect.

The presented approach for the FEM modelling of the nanocomposite structures allows to predict mechanical properties of its different variants before the real material will be created, what can significantly increase the efficiency of the new materials designing^{9,10}.

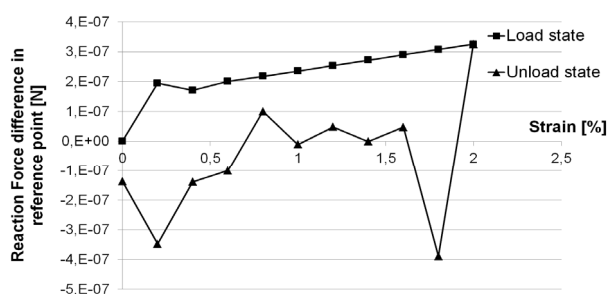


Fig. 2. Values of differences of the reaction forces between TiC-steel and TiC+TiB₂+B₄C-steel composites

3. Conclusion

Nanoindentation tests have shown that the hardness and elastic modulus increase in following order: 316L steel, TiC/steel and (Ti-B-C)/steel nanocomposites respectively.

The numerical analysis showed that the composites stiffness is noticeably higher in comparison to the steel. The mechanical properties (stiffness) of the composite with boron presence are better (higher stiffness) in comparison to the steel and composite with TiC. The presented differences in values of reaction force are small. This results from the small sizes of analysed structures.

Financial support of the work by the Ministry of Science and Higher Education within the project No. NR15-0067-10/2010-2013, is gratefully acknowledged.

REFERENCES

1. Alizadeh A., Nassaj E. T., Ehsani N.: J. Eur. Ceram. Soc. 24, 3277 (2004).
2. Sinha A., Mahata T., Sharma B. P.: J. Nucl. Mater. 301, 165 (2002).
3. Gursoy A., Ferhat K., Servet T.: J. Eur. Ceram. Soc. 23, 1243 (2003).
4. Matkovich V. I., Samsonov G. V., Hagenmuller P., Lundstrom T.: *Boron and Refractory Borides*, Springer-Verlag, New York 1977.
5. Vallauri D., Atias Adrian I. C., Chrysanthou A.: J. Eur. Ceram. Soc. 28, 1697 (2008).
6. Biedunkiewicz A., Biedunkiewicz W., Figiel P., Grzesiak D.: Chem. Listy 105, s767 (2011).
7. Biedunkiewicz A., Wysiecki M., Noworol P.: Polish Patent: *Organotitanium precursor and method of producing and processing of organotitanium precursor* P200978 (2008).
8. Biedunkiewicz A., Figiel P., Gabriel U., Sabara M., Lenart S.: Cent. Eur. J. Phys. 9, 417 (2011).
9. Zubko P., Pesek L., Bláhová O.: Chem. Listy 105, s664 (2011).
10. Hausild P., Nohava J., Materna A.: Chem. Listy 105, s676 (2011).

A. Biedunkiewicz, W. Biedunkiewicz, P. Figiel, and D. Grzesiak, (West Pomeranian University of Technology, Szczecin, Poland): Numerical Modelling of the Nanocomposites in Steel/Ti-B-C System

The Selective Laser Sintering/Melting process was used to prepare Ti-B-C/316L stainless steel nanocomposite materials. Hardness and elastic modulus measurements were performed on MTS Nano Indenter XP. The differences in mechanical properties between steel, 316L steel/TiC and 316L steel/Ti-B-C composites based on the results of modelling by numerical method have been presented.

ASSESSMENT OF THE CRITICAL PLACES IN THE CASTED PISTON BASED ON A LOCAL STRENGTH – MICROSTRUCTURE MODEL

PETER BIGOŠ^a, MICHAL PUŠKÁR^a,
and LADISLAV PEŠEK^b

^a Department of Machine Design, Transport and Logistics,
Faculty of Mechanical Engineering,

^b Department of Material Science, Faculty of Metallurgy,
TU in Košice, Letná 9, 040 01 Košice, Slovak Republic
michal.puskar@tuke.sk

Keywords: local strength, secondary dendrite arm spacing – SDAS, FEM

1. Introduction

A failure of construction elements depends on the position of a critical place and its local mechanical properties which are related to processing technology of the given machine part. In the case of a casted piston of two-stroke combustion engine, the local mechanical properties are affected predominately by the casting technology^{1,2}. The decisive factors are especially: tension strength, critical deformation, modulus of elasticity, fatigue strength. These factors are influenced greatly by the casting method³. A cooling rate during casting is the most important factor with regard to material microstructure and its mechanical characteristics. An ultimate tensile strength (UTS) correlates well with the secondary dendrite arm spacing (SDAS)⁴. During the evaluation of reliability an assumption that the mechanical properties of material are homogenous is usually taken into consideration. However, the real differences in microstructure cause a variability of mechanical characteristics in individual localities of the same material.

Pistons of combustion engines are usually made of the near eutectic aluminium-silicon alloys. Since the microstructure of a cast differs in its various areas, there are also different values of mechanical properties and it is insufficient to take into consideration the mechanical characteristics of the global cast material.

One of the possibilities how to determine the ultimate tensile strength is based on the secondary dendrite arm spacing (SDAS). There are well-known relations between the tensile strength and microstructure of silumins⁵:

$$UTS = 270 - 1.4399 \text{ SDAS} \quad (1)$$

where: UTS – ultimate tensile strength [MPa], SDAS – secondary dendrite arm spacing [μm].

The main purpose of this work is to determine the local values of the strength by means of metallographic analysis, as well as to define the critical areas of the piston using a finite element analysis.

2. Experiments

The gravity casted piston of the company Vertex made from near eutectic aluminium-silicon alloy was provided for this study. The piston was cut into two cross-section parts. The samples were prepared from its various areas in order to apply metallographic light microscopy which enables a statistical analysis of microstructure. The secondary dendrite arm spacing (SDAS) was measured in specific parts of the piston by identifying and measuring small groups of well-defined secondary dendrite arms on the screen of the image analyzer.

$$SDAS = d/n \quad (2)$$

where: d – length of the line drawn from edge to edge of measured arms, n – number of dendrite arms.

The volume fractions of the constituents were quantified with the image analysis (Fig. 1) of the microstructure.

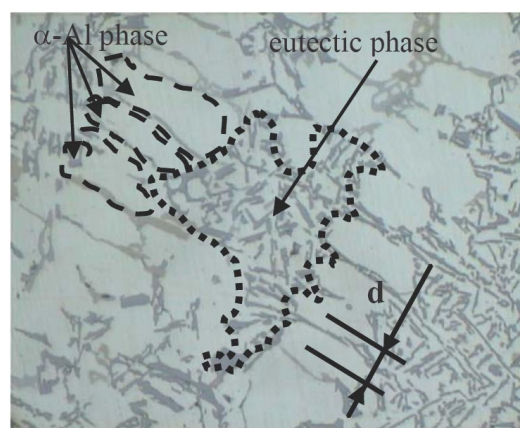


Fig. 1. Microstructure of silumin

The values of von Mises stress, σ_{VM} , were determined in the next step in the selected areas of the piston by means of the FEM using the Cosmos software. The material was considered to be elastic and the dimensions of analysed positions (Fig. 2) were from several hundreds μm to 1 mm in the size.

3. Results of measurement

The values of the secondary dendrites arm spacing in individual areas of the microstructure are presented on Fig. 3. The difference between the minimal value (24 μm) and the maximal value (47 μm) is 96 %. From a quantification of the constituent phases, Fig. 4, results that the volumetric share of eutectics increases from the position 1 (upper position) to the position 5 gradually (position of

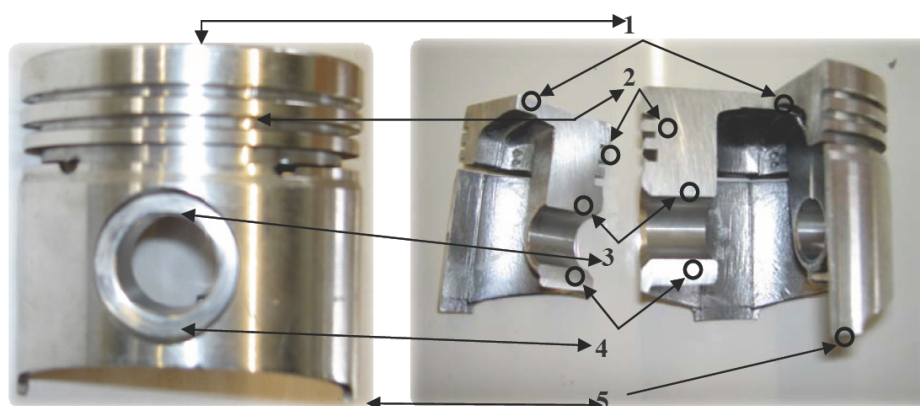


Fig. 2. Analyzed positions in the piston: 1. upper surface (US), 2. piston rings (PR), 3. pin (P), 4. Seeger ring (SR), 5. sealing flap (SF)

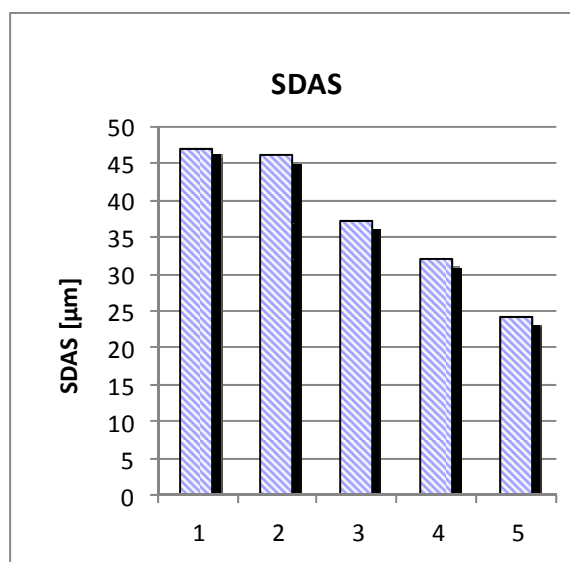


Fig. 3. SDAS values for specific individual analysed positions

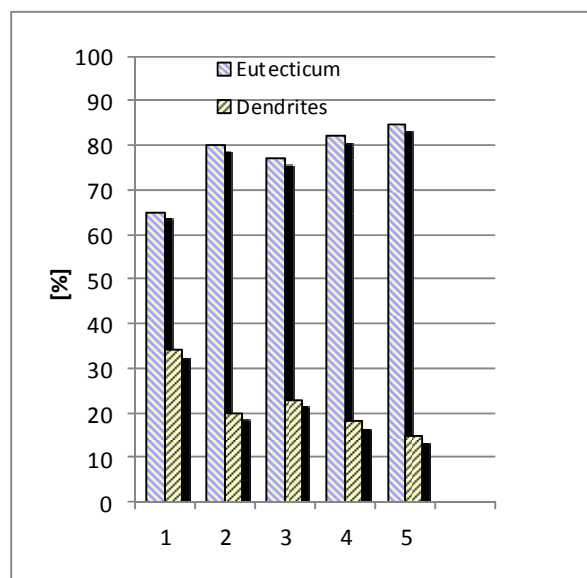


Fig. 4. Quantification of constituent phases

sealing flap). A supplement to the 100 % of the whole creates the dendrite α -phase. Analysing together the volume fraction of the eutectic phase with the SDAS results it is interesting to highlight the fact that a relation exists between them: the region with higher values of the SDAS has got a small amount of eutectic phase and reverse the region with the smaller values of the SDAS has got higher values of the eutectic phase.

4. Discussion

The critical positions are such places where the ratio between the local loading stress and the local strength is the highest.

Thus, estimative prediction of the cast aluminium component properties should be made based on local material mechanical properties, which enables to calculate the ratio of stress vs. ultimate tensile strength. Local mechanical properties may be obtained by local metallographic analysis.

The ultimate tensile strength UTS_{SDAS} was then calculated from experimentally determined values of SDAS according relation (1) in all specific positions 1–5. The results of microstructure evaluation (SDAS) and local strength value UTS_{SDAS} are presented in the Tab. I. It can be seen that there is a change in SDAS of about 100%, as occurs between positions 5 and 1, and that it is equivalent

Table I
Measured and calculated values of SDAS and load for different positions in the piston

Position	SDAS [μm]	UTS _{SDAS} [MPa]	σ_{FEM} [MPa]	$\sigma_{\text{FEM}} / \text{UTS}_{\text{SDAS,max global}}$	$\sigma_{\text{FEM}} / \text{UTS}_{\text{SDAS local}}$	local-global [%]
1 upper surface	47.0	202	56	0.237	0.277	16.7
2 piston rings	45.6	204	78.4	0.332	0.384	15.6
3 pin	37.9	215	96	0.407	0.446	9.6
4 Seeger ring	31.5	225	44	0.186	0.196	5.1
5 sealing flap	23.6	236	21.2	0.080	0.090	0.1

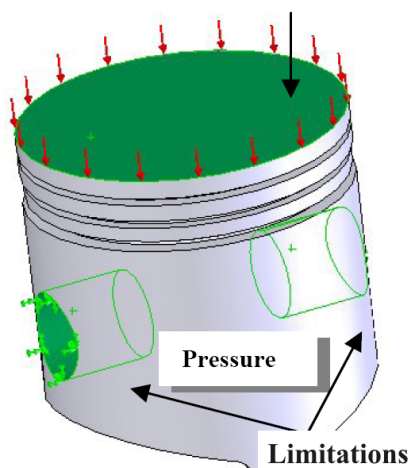


Fig. 5. Pressures and limitations applied on piston surfaces

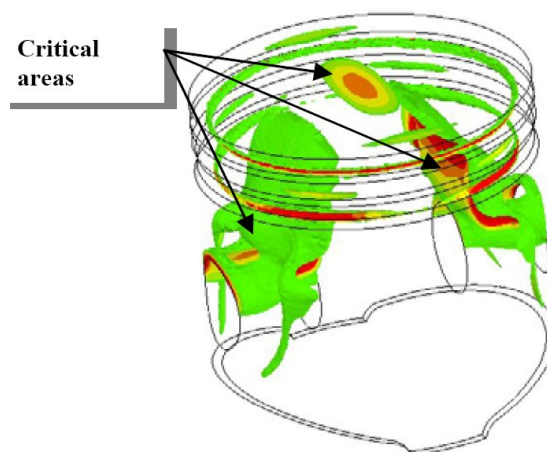


Fig. 6. Stress distribution in critical positions

to significant changes in UTS, e.g. the stress level changes from about 236 to 202 MPa (about 17 %).

The FEM stress analysis⁶ of the loaded piston, Fig. 5, proved that there are predominately two important critical areas with high stress: the upper holes of the piston pin (3) and the piston head (1) with the piston rings (2), Fig. 6. The stress values σ_{FEM} for each of the piston position (Fig. 2) obtained by means of the FEM are in Tab. I.

A global design uses only one material value for the whole component, e.g. the UTS=236 MPa for the microstructure with the highest strength. The corresponding relative load $\sigma_{\text{FEM}} / \text{UTS}_{\text{SDAS,max}}$ is in the 4th column in the Tab. I. These values are different from those obtained by means of a local approach which are the values of the stress σ_{FEM} related to the real ultimate tensile stress values UTS_{SDAS} obtained by the metallographic way based on the SDAS in different positions of the component, $\sigma_{\text{FEM}} / \text{UTS}_{\text{SDAS}}$, Tab. I, 5th column. The difference between local and global approach can reach up to 16.7 %.

These differences can be relevant mainly in the case of fatigue loading, in this case also changes of positions of the critical areas can be expected⁷.

5. Conclusions

The values of local strength were determined in selected specific positions of piston casted from the silumin alloy based on relation between UTS and microstructure parameter SDAS. The difference between local and global approach reach up to 17 % for selected positions of the whole component. Ignoring the real local load can cause an early failure of component.

This study was supported by the grant tasks „VEGA 1/0356/11 Innovative Processes in Design of Driving Units for Transport Machines and Optimisation of Material Flows and Logistics in Order to Save Energy and to Increase Reliability for Application Purposes in Practice“ and „Research Centrum for Control of Technical, Environmental and Human Risks for Sustainable Development of Production and Products in Engineering“.

REFERENCES

1. Bigoš P., Puškár M.: *Strojárstvo* 50, 2 (2008).
2. Kovařík L., Ferencey V., Skalský R., Částek L.: *Konstrukce vozidlových spalovacích motorů*. Naše vojsko,

- Praha 1992.
3. Juliš M. et al.: Chem. Listy 105, 812 (2011).
 4. Lim C. S., Clegg A. J., Loh N. L.: J. Mater. Proces. Technol. 70, 99 (1997).
 5. Takahashi T., Sugimura Y., Sasaki K.: J. Manuf. Sci. Eng. 126, 25 (2004).
 6. Puškár M., Bigoš P.: Strojárstvo 52, 5 (2010).
 7. Stroppe H.: Materialwissenschaft und Werkstofftechnik 40, 738 (2009).

P. Bigoš, M. Puškár, and L. Pešek (*Technical university of Košice, Košice, Slovak Republic*): **Assessment of the Critical Places in the Casted Piston Based on a Local Strength – Microstructure Model**

The study analyses the critical positions in the combustion engine pistons produced by gravity casting of near eutectic aluminium-silicon alloys. The local strength in various positions was calculated from secondary dendrite arm spacing in the microstructure, the real local load was calculated via finite element analysis. The global strength approach uses one strength value for the whole component, while the local approach uses the local strength values depending on local microstructure. The difference between both local and global strength approach can reach up to 17 %.

CHANGE IN PROPERTIES OF HVOF COATINGS UNDER CONDITIONS OF THERMAL CYCLIC LOADING

JANETTE BREZINOVÁ,
ANNA GUZANOVÁ, and MARIÁN EGRI

*Technical University of Košice, Faculty of Mechanical Engineering, Mäsiarska 74, 040 01 Košice, Slovak Republic
janette.brezinova@tuke.sk*

Keywords: HVOF coatings, high temperature cyclic loading, microhardness

1. Introduction

Thermally-sprayed coatings belong to the dynamically developing field of surface engineering^{1,2}. These high-quality functional coatings are applied in the basic industry, as well as in renovations³, mainly due to their excellent properties, which are characterized by high wear resistance^{4–8}, corrosion resistance and resistance against high temperatures^{9,10}. Thanks to a wide range of different combinations of coating–substrate materials, thermal spraying offers as many possibilities as no other technology of coatings deposition. HVOF (High Velocity Oxygen Fuel) is one of the technologies, which form coatings with very low porosity (<1 %) compared with the basic material and with high adhesion strength (> 80 MPa). The substrate undergoes minimal thermal changes during spraying. The roughness of the resulting coating surface is low.

Thanks wide variety of suitable materials and their combinations, the area of utilization thermally sprayed coatings is very broad. It is possible to deposit coatings of various materials from pure metals to special alloys. Properties of cermet-based coatings are given by the type, morphology and size of hard particles and their volume fraction in tough matrix.

This paper presents results of assessment of HVOF coatings. The coatings were subjected to cyclic thermal stress. Their tribological properties were evaluated under conditions of erosive wear. The quality of coatings was measured by pull-off testing, microhardness testing, and by EDX analysis. The experimental conditions were set to simulate the operating conditions of iron manufacturing in a basic oxygen furnace (BOF).

2. Materials and methods

The substrate for application of the coatings was C15E carbon steel (STN 41 2020, 12 020, 1.1141). Chemical composition of the steel is listed in Tab. I.

Table I
Chemical composition of the steel substrate (mass %)

C	Mn	Si	P	S
0.12–0.18	0.30–0.60	0.15–0.40	max 0.035	max 0.035

Mechanical properties of the steel substrate: tensile strength 740–880 MPa, yield strength \geq 440 MPa. The test samples were made from \varnothing 50 mm round bar with a length of 15 mm.

Substrate pre-treatment: test samples were pre-treated by air grit blasting at air pressure of 0.5 MPa with brown corundum with a grain size of 1.00 mm.

Three types of coatings were deposited by HVOF technology on pretreated samples: WC-729-1/1343 VM (WC-17Co), WC-731-1/1350 VM (WC-Co-Cr) and CRC-300-1/1375 VM (Cr₃C₂-25NiCr). Materials were supplied in the form of powder, agglomerated and sintered, produced by Praxair, Inc., USA. Tab. II shows chemical compositions of the powders.

Table II
Chemical compositions of the powders sprayed

Coating	C	Co	Fe	W	Cr	Ni
C-17Co 1343	5.5	16.2	0.036	78.4	–	–
WC-Co- Cr 1350	5.5	9.9	0.02	80.58	3.9	–
Cr ₃ C ₂ - 25NiCr 1375	10	–	–	–	68.5	21

The equipment JP-5000, Praxair TA employed in the experiment uses the HP/HVOF (High Pressure / High Velocity Oxygen Fuel) process with System Powder Feeder 1264. The surface of deposited coatings was not conditioned after spraying. Spraying parameters are listed in Tab. III.

The thickness of coatings was determined by a magnetic thickness gauge. Adhesion of coatings was evaluated by the pull-off test according to STN EN 582 using a tensile machine ZDM 10/91.

After the pull-off adhesion test, the tensile stress required to sever the weakest inter-phase bond (adhesive fracture) or to rupture the weakest structure component (cohesive fracture) was determined and fractographic assessment was performed.

Table III
Parameters of spraying

Particle velocity	Adhesion	Oxide content	Porosity	Deposition power	Typical coating thickness
[m/s]	[MPa]	[%]	[%]	[kg/h]	[mm]
600 - 1000	< 70	1 - 2	1 - 2	3 - 6	0.2 - 2

Microhardness was measured according to STN ISO 4516 on Shimadzu HMV-2E test equipment, with the load of 980.7 mN (100 g) and a dwell time of 15 s. Samples were subjected to cyclic thermal load in an electric chamber furnace according to the following schedule:

1. heating to 900 °C,
2. dwell in the furnace for 20 minutes,
3. cooling of samples in still air to ambient temperature.

Samples were subjected to 10 thermal cycles. After the 3rd, 5th, 8th and 10th thermal cycle, samples were collected to evaluate the adhesion of coatings. Structure and chemical composition of coatings were studied using the scanning electron microscope (SEM) JEOL JSM – 7000 F with INCA EDX analyzer for local chemical analysis.

To simulate the process conditions in BOF (impact and flow of oxides in BOF gas), the coatings were subjected to erosion wear at abrasive impact angles of 45° and 75°. To simulate the process of oxide impact, a laboratory mechanical blasting device KP-1 was used that allows the circulation of abrasive to be monitored. The abrasive used – brown corundum (Al₂O₃) had a grain size of 1 mm. The intensity of coatings' wear was evaluated using gravimetry (mass loss of the coating). Peripheral speed of the blasting wheel was 5.0 m s⁻¹ and the exit speed of abrasive was 70.98 m s⁻¹.

3. Results and discussion

Thicknesses of the as-sprayed coatings were as follows: 1343–234 μm, 1350–356 μm and 1375–393 μm. The highest microhardness values (Fig. 1) was found in the coating 1350 (1447 HV 0.1). It was due to a high content of tungsten and an addition of cobalt. In comparison, the coating 1343 contains tungsten at lower concentration and showed a lower value of microhardness (1010 HV 0.1). The lowest microhardness values were found in the coating 1375, which has a high content of chromium and is tungsten-free (975 HV 0.1).

Thermal cycles caused changes in microhardness of specimens. The most significant change occurred in the coating 1343. The hardness of the coating 1375 decreased, whereas that of the coating 1350 slightly increased. These values are related to structural changes in the coatings.

Fig. 2 shows fracture surfaces and the appearance of surfaces of the coatings upon thermal cycles.

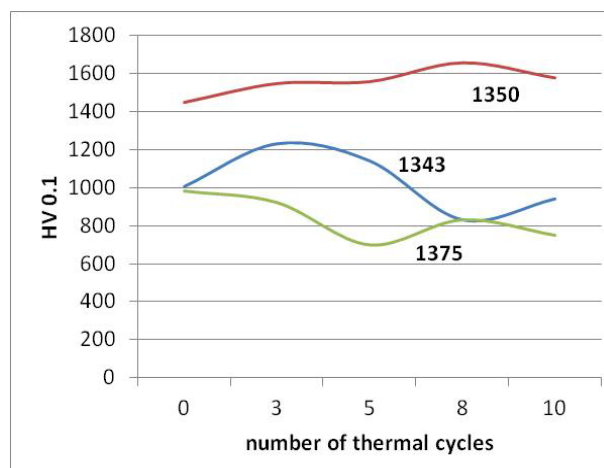


Fig. 1. Trend in microhardness in coatings

EDX spectral analysis of the coating 1343 revealed the presence of two basic phases – solid WC particles and cobalt, which is in line with the chemical composition of the powder. EDX spectral analysis of the coating 1350 showed the presence of WC particles, chrome and cobalt matrix, in which WC particles were embedded. EDX spectral analysis of the coating 1375 confirmed the presence of large particles of Cr₃C₂ and the prevailing component of the coating 1375: nickel-chromium matrix. The matrix and hard particles of WC and Cr₃C₂ are well visible on fractures of the coatings, Fig. 2.

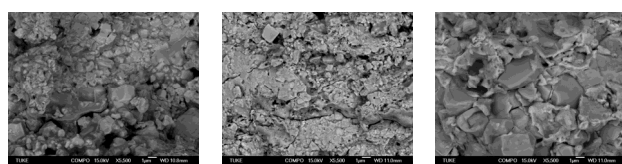
Despite its high hardness, the coating 1350 suffered thermal cracking after 3 thermal cycles, as seen in Fig. 2 – showing the surface after thermal cycles. The surface of coating 1343 covered with a layer of blue oxides and showed strong chalking during the thermal cyclic loading. The coating 1375 retained its aesthetic and tactile qualities after thermal cycles. The appearance of surfaces of coatings during thermal cyclic loading and the character of their fractures are also shown in Fig. 2. Results of the evaluation of coatings adhesion are shown in Fig. 3.

The adhesion of coatings already decreased after three thermal cycles but then it remained almost constant during subsequent thermal loading.

The coating 1375 did not fracture in the pull-off test. Its adhesion may therefore be considered to be higher than the value listed.

Fig. 4 depicts the dependence of erosive wear on impact angles of abrasive. For all types of coatings, very similar dependences were observed. Higher weight losses were recorded at an impact angle of 75° in all types of coatings. Literature data suggest that hard materials, such as the coatings suffer heavier wear at larger impact angles. This was confirmed by the experiment.

The intensity of erosive wear is influenced by the ratio of the coating – abrasive hardnesses and by the structural characteristics of the coating. Wear intensities in all coatings were almost identical, being higher at the impact angle of 75°. More complex surface states were reached at



Fractures of coatings (SEM)



Surfaces of coatings after 10 thermal cycles (mag. 50x)

1343

1350

1375

Fig. 2. Fractures and appearance of surfaces of coatings after thermal cycles

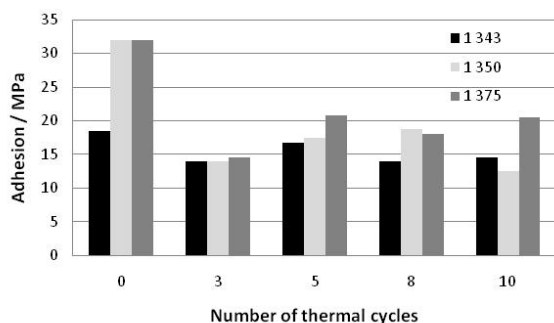


Fig. 3. Adhesion of coatings after thermal cycles

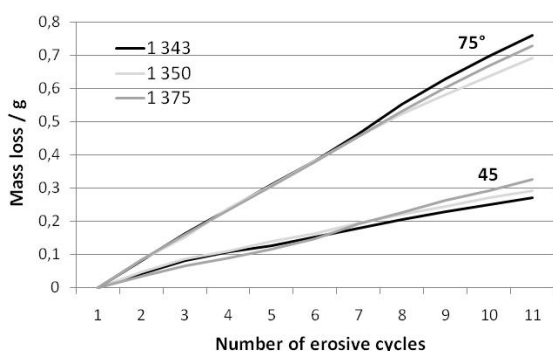


Fig. 4. Erosive wear of coatings

75° impact angle, material was removed and new surface configuration followed the direction and shape of the incident abrasive.

At larger impact angles, the forging effect of the abrasive prevails, whereas at smaller impact angles, the grooving effect dominates.

4. Conclusion

The coating 1350 (1447 HV 0.1) showed the highest hardness, whereas the coating 1375 (975 HV 0.1) showed the lowest hardness value. The coating 1350 cannot be used in the environment of BOF with high and fluctuating temperatures because of it cracks after a few thermal cycles. This would disrupt its protective function and allow high temperature corrosion of the substrate. At high temperatures, the coating 1343 showed strong chalking. This may cause significant losses in weight (and consequently in thickness) of the coating and reduce its durability. The coating 1375 showed lower hardness than others, retained its integrity and adhesion during thermal cyclic loading. No other qualitative changes occurred in this material. Its resistance to erosive wear was equal to that of the other coatings.

Based on the experimental results obtained the recommend for renovation of components operating under extremely high and cyclic temperatures and erosion wear condition would be the coating 1 375 ($\text{Cr}_3\text{C}_2\text{-25NiCr}$).

This paper is a result of the project: “Unique equipment for evaluation of tribocorrosion properties of the mechanical parts surfaces“ (ITMS: 26220220048) supported by the Research & Development Operational Programme funded by the ERDF and Grant Scientific Project KEGA No. 059TUKE-4/2012.

REFERENCES

- Sololenko O. P.: *Thermal Plasma Torches and Technologies*. Cambridge international science publishing, Cambridge 2000.
- Suryanarayanan R.: *Plasma Spraying: Theory and Applications*. CNRS, London 1993.
- Tan J. C. L., Looney M. S. J., Hashmi: *J. Mater. Process. Technol.* 92-93, 203 (1999).
- Kašparová M., Zahálka F., Houdková Š.: *Proceedings from conference METAL*, Hradec nad Moravicí, pp.1-4 (2009).
- Kupková M., Jakuběczyová D., Hagarová M.: *Metallurgija* 49, 203 (2010).
- Bidulský R., Actis Grande M., Bidulská J., Vlado M., Kvačkaj T.: *High Temperature Materials and Processes* 28, 175 (2009).
- Guilemany J. M., Miguel J. M., Vizcaino S., Lorenzana C., Delgado J., Sánchez J.: *Surf. Coat. Technol.* 157, 207 (2002).
- Ábel M.: *Transfer inovácií* 10, 157 (2007).
- Matthews S., James B., Hyland M.: *Surf. Coat. Tech-*

no. 203, 1086 (2009).

10. Li J. F. Li, Ding L. C. X.: Mater. Sci. Eng. A 394, 229 (2005).

J. Brezinová, A. Guzanová, and M. Egri (*Technical University of Košice, Faculty of Mechanical Engineering, Department of Technology and Materials, Slovakia*):
Change in Properties of HVOF Coatings under Conditions of Thermal Cyclic Loading

This contribution presents interim results of evaluation of changes in local mechanical properties of HVOF coatings. The research was aimed at changes in microhardness of composite coatings deposited by the high velocity oxygen fuel process. The evaluated coatings were subjected to high-temperature cyclic loading. Microhardness of the coatings was measured on cross-sections of samples. Three types of coatings based on WC-Co, WC-Co-Cr and Cr₃C₂-25NiCr were examined. Their microstructure was studied using SEM-EDX techniques.

EFFECT OF WORKING TEMPERATURES ON PROPERTIES OF CONTINUOUS STEEL CASTING ROLLS CLADDING LAYERS

JANETTE BREZINOVÁ, JÁN VIŇÁŠ,
and DENISA LORINCOVÁ

Technical University of Košice, Faculty of Mechanical Engineering, Mäsiarska 74, 040 01 Košice, Slovak Republic
janette.brezinova@tuke.sk

Keywords: cladding, renovation, continuous casting rolls, layer structure, microhardness, thermal loading

Introduction

Continuous casting rolls provide of slab movement in the line and are therefore the key equipment of a line for continuous casting of steel. Their reliable operation is closely associated with their lifetime, which can be extended by renovation^{1–4}.

Wear affecting rolls in continuous casting of steel is illustrated in Fig. 1 and Fig. 2 depends on the location of the rolls in the continuous casting line, on the temperature of cast slabs, surface temperature of the rolls, method of cooling, cooling water quality and other factors.

The paper explores the impact of heating cycles on micro-hardness of cladding layers.

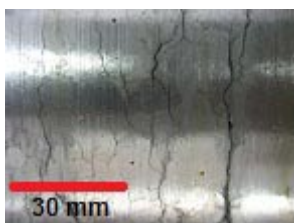


Fig. 1. Surface of the roll: the crack caused by thermal fatigue



Fig. 2. Exfoliation of cladding layers caused by combined loads

Experimental

The continuous casting roll of 180 mm in diameter examined in this study was renovated by welding. The roll was part of the curvilinear section of the continuous casting line shown in Fig. 3. It was made from forged steel 41CrMo4 EN 10083-1-91 with chemical composition given in Table I.

Table I

Chemical composition of steel 41CrMo4 roll EN 10083-1-91 (in wt. %), balance of Fe

C	Mn	Si	Cr	Ni	Mo	P	S	Fe
0.41	0.63	0.26	1.12	0.27	0.18	0.017	0.015	bal.

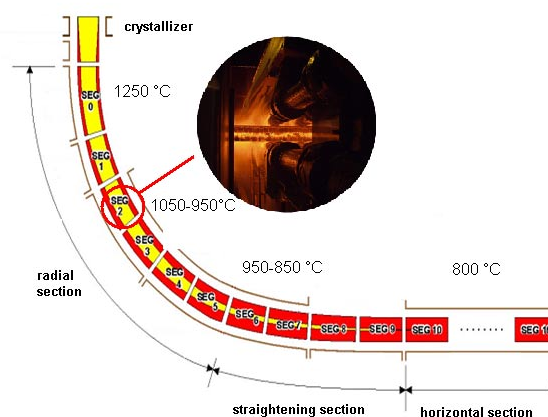


Fig. 3. Continuous casting line

The three-layer weld cladding was created on the surface of the roll by submerged arc welding technology (SAW) according to EN ISO 121 4063. The clad was created without an interlayer, using Weldclad GU125LZ – COREWIRE equipment. This device allows welding

Table II

Chemical composition of weld wires (in wt. %), Fe bal.

Element	Wire		
	A	B	C
C	0.1	0.25	0.3
Si	0.6	0.6	0.6
Mn	1.0	1.0	1.0
Ni	2.5	0.25	–
Cr	12.2	9.0	12.2
Mo	0.8	2.0	0.75
Nb	0.15	–	–
Cu	–	–	–
V	0,15	–	0,15

Table III
Chemical composition of the universal flux (in wt. %)

(SiO ₂ + TiO ₂)	(Al ₂ O ₃ + MnO)	(CaO+MgO)	(CaF ₂)
20	17	38	19

parameters to be changed in the course of rotation of the roll during the renovation.

Weld wires W3-WLDC3 (A), W5HT-WLDC 5Mod (B) and W8-WLDC8 (C) with a diameter 3.2 mm from COREWIRE, Ltd., UK were used for making the claddings. Chemical compositions of the wires (as declared by the manufacturer) are given in Table II.

Universal flux suitable for weld wires with iron content of up to 50 % was used. Its chemical composition is given in Table III.

Prior to cladding, the roll was preheated to 400 °C. After cladding, it was wrapped and cooled to room temperature. Then it was pre-heated in furnace at 500 °C and held for 8 hours, then slowly cooled in the furnace. Welding parameters are listed in Table IV.

The samples for metallographic analysis, thermal cycles and microhardness testing were taken from the renovated roll's surface.

Microhardness was measured by Vickers method, described in the standard STN EN 1043-2, on SHIMADZU HMV-2 on polished transverse metallographic sections. The work load was 980.7 mN (HV 0.1). Test samples were exposed to thermal cycles at 900 °C for 120 s.

Table IV
Cladding parameters

Wire	Voltage [V]	Current [A]	Oscillation [mm]
A	28	450	45
B	26	600	47
C	26	450	50

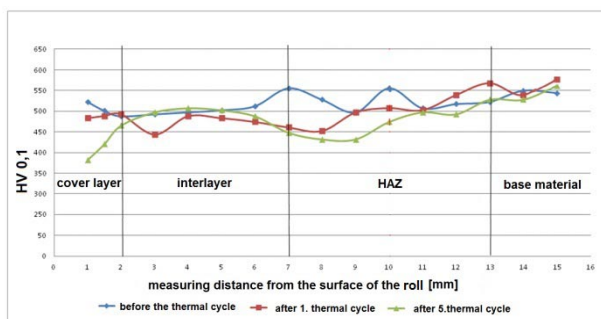


Fig. 4. Microhardness before and during thermal load measured on cladding made by weld wire A

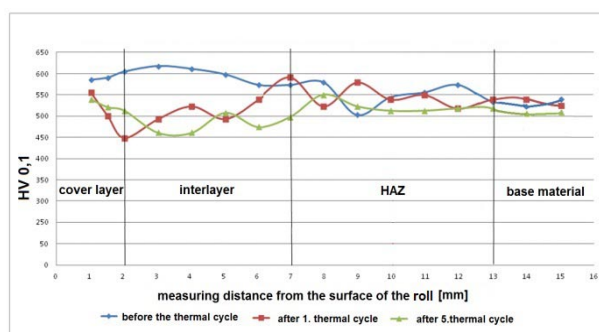


Fig. 5. Microhardness before and during thermal load measured on cladding made by weld wire B

Subsequently, the samples were cooled in water at 18 °C.

Fig. 4, 5 and 6 document cladding microhardness before the thermal load and upon the first and the fifth thermal cycle.

The highest values of microhardness during thermal cycles were measured in the cladding made of welding wire C – 600 HV 0.1. Microhardness value is consistent with the chemical composition of the welding wire, especially with the highest carbon content and also high chromium content among the evaluated additional materials.

Due to thermal cycles, microhardness values of all weld deposits decreased. The cladding made of weld wire A decreased about 150 HV 0.1, the cladding made of weld wire B to 60 HV 0.1 and cladding made of weld wire C there was found the decrease of microhardness of 130 HV 0.1 in comparison with measured values before thermal cycles. The decline of microhardness values continued depending on the number of thermal cycles in all tested weld deposits. As for the microhardness values measured in the interlayer of cladding A, thermal cycles had not a major impact, but the microhardness of B and C weld deposits decreased compared to microhardness values measured before the thermal stress.

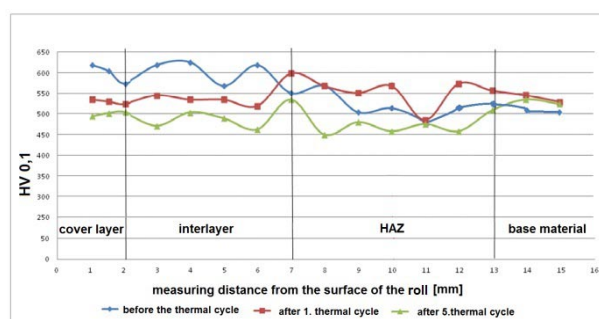


Fig. 6. Microhardness before and during thermal load measured on cladding made by weld wire C

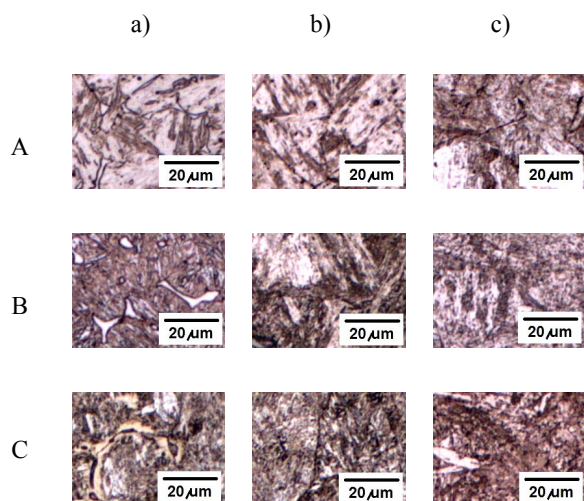


Fig. 7. Structures of weld clad A, B, C before the thermal stress

The microhardness values measured in HAZ are in the range of 500 to 600 HV 0.1, which correspond to the chemical composition and used cladding parameters. The higher hardness was found in HAZ of cladding B.

The microscopic analysis of each layer in renovated rolls was performed using light microscopy.

The structure of the base material of the roll is formed by coarse-grained martensite. Results of microscopic analysis are presented in Fig. 7.

Fig. 7b presents the structural analysis of interlayer weld clad A, B, C, which is fine-grained martensite. The structure of heat affected zone (HAZ) is documented in Fig. 7c and consists of low-carbon martensite.

Identified microstructure corresponds to the chemical composition of additional materials. Cover layer of weld A is formed by a low-carbon martensite-ferrite structure. Cover layer of weld B and C also has a ferrite-martensite structure, with less distinct grain boundaries. In the structure the presence of carbide precipitates has been reported. Based on the chemical composition of additional materials, especially Cr and Ni, content of the precipitates is of the type M_3C and M_7C_3 (ref.^{4,5}). Molybdenum and other alloying elements, such as tungsten, vanadium and niobium precipitate in the M_7C_3 , $M_{23}C_6$ and M_6C eutectic carbides and also carbides (e.g. Mo_2C , VC), which is consistent with the ref.^{6–10}. The microstructure of the interlayer is formed martensite – ferrite structure as well. The HAZ has documented martensite of coarse texture.

3. Conclusion

Based on experiments realized by the evaluation of local mechanical properties of cladding metal parts and the HAZ can be concluded that the weld made by additional material B (W5HT-5Mod WLDC) resisted thermal cyclic stresses the best. The cover layer which is in practice sub-

jected to the most intense tribodegradation effects decreased its microhardness of 60 HV 0.1, while the additional material A decreased of 150 HV 0.1 and C decreased of 130 HV 0.1. The measured values correspond to the martensite structure of precipitation hardened ferritic carbides of M_3C and M_7C_3 type.

The contribution was elaborated within the Research Project KEGA No. 059TUKE-4/2012 and within the Research Project ITMS 26220120060 – Management Research Centre for technical, environmental and human risks to continuous development and production of products in engineering.

REFERENCES

1. Čomaj M., Šefčík D.: *Proceedings from conference Welding 99*, Tatranská Lomnica, 68–71 (1999).
2. Kamenský M.: *Zváranie XIX*, 9–10, 315–316 (1970).
3. Viňáš J., Kaščák Ľ.: *Bull. Mat. Sci.* 31, 125 (2008).
4. Viňáš J.: *Dissertation*. Technical University of Košice, Košice 2003.
5. Durand-Charre M.: *Microstructure of steels and Cast Irons*. Springer-Verlag, Berlin 2003.
6. Kovaříková I., Szewczyková B., Blaškovič P., Hodúlová E., Lechovič E.: *Mater. Sci. Technol.* 9, 1 (2009).
7. Knoško P., Kovaříková I., Hodúlová E.: *Science work MtF STU 25*, 83 (2008).
8. Knoško P., Blaškovič P., Kovaříková I.: *Proceedings from conference Zváranie 2007*, 196–199 (2007).
9. Čabelka J.: 'Weldability of metals and alloys' VEDA, 1977.
10. Kotus M., Andrássová Z., Čičo P., Fries J., Hrabě P.: *Res. Agr. Eng.* 57, 74 (2011).

J. Brezinová, J. Viňáš, and D. Lorincová
(*Technical University of Košice, Faculty of Mechanical Engineering, Department of Technology and Materials, Slovakia*): **Effect of Working Temperatures on Properties of Continuous Steel Casting Rolls Cladding Layers**

This contribution deals with properties evaluation of cladding layers realized by SAW - submerged arc welding 121 STN EN ISO 4063. Worn roll comes from curved sector of continual steel casting line and was made of material 41CrMo4 EN 10083-1-91 by forging. There were three cladding layers deposited on the roll surface. For the renovation of the roll following welding wires were used W3-WLDC3, W5HT-WLDC 5Mod a W8-WLDC8, diameter \varnothing 3.2 mm. Mixing of cladding layers and their microstructure using light microscopy were evaluated. On the created welds microhardness of the base material, heat-affected area and cover area of the weld in the initial state and after the exploitation in simulated work environment was assessed. Heat cycles corresponded to work conditions of continuous casting rolls.

MECHANICAL PROPERTIES AND MICROSTRUCTURE OF MODEL LEAD-FREE JOINTS FOR ELECTRONICS MADE WITH USE OF NANOPOWDERS

JIRÍ BURŠÍK^a, VILMA BURŠÍKOVÁ^{b,c},
ZBYNĚK PEŠINA^d, and JIRÍ SOPOUŠEK^e

^a Institute of Physics of Materials, Academy of Sciences of the Czech Republic, Žitkova 22, 616 62 Brno, ^b Masaryk University, Faculty of Science, Regional R&D center for low-cost plasma and nanotechnology surface modifications, Kotlářská 2, 611 37 Brno, ^c Masaryk University, CEITEC, Kotlářská 2, 611 37 Brno, ^d Brno University of Technology, Faculty of Mechanical Engineering, Technická 2, 616 69 Brno, ^e Masaryk University, Faculty of Science, Department of Chemistry, Kotlářská 2, 611 37 Brno, Czech Republic
bursik@ipm.cz

Keywords: solder, silver nanopowder, nanoindentation

1. Introduction

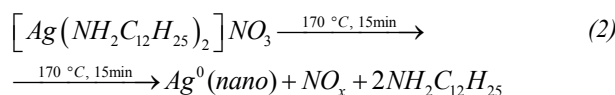
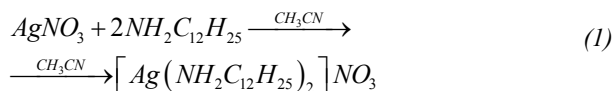
Based on EU legislative, classical solders based on lead and tin are being replaced by their lead-free alternatives with the obvious aim to reduce health risks and environmental problems. The search for a replacement solder material has been underway for some time and a number of formulations are already in use¹. However, solutions presently used have often reliability problems caused by worse mechanical properties, higher tendency to oxidation and higher melting temperature. After a decade of research it is now an accepted fact that there is no universal replacement for the traditional lead-tin solder.

Nanoparticles of pure metals and alloys exhibit the depression of melting point compared to bulk materials², hence they are able to aggregate and to form firm interlayer joints at low temperatures. Exploiting this effect in soldering industry can save energy, work and materials, and in particular it may subscribe to the solution of the above last mentioned problem³.

In this work, Ag nanopowders were prepared as potential low-toxic constituents of novel solders by a chemical wet synthesis with the aim to study the effect of melting temperature depression and to evaluate the mechanical properties of sintered layers prepared in various annealing regimes.

2. Experimental

Chemical wet synthesis of Ag nanoparticles proceeded in two steps. At first the complex of AgNO₃ with dodecylamine was prepared in acetonitrile and subsequently it was broken down at elevated temperature (170 °C):



Resulting nanoparticles were separated as a solid product and stored in a toluene bath. They were characterized using a Philips CM12 STEM transmission electron microscope (TEM). Model joints, i.e. sandwiches consisting of thin copper plates with Ag nanopowder interlayer were prepared and annealed at various temperatures (see Table I). Samples 3, 4 and 5 were heated up inside the furnace from the room temperature at 15 K min⁻¹ rate (marked as “ramp” in the Table; heating time is not included in the annealing time in the Table); the other samples were placed in the furnace already at the declared temperature (marked as “flash”). After annealing the samples were let in the furnace to cool down. Metallographic cross-sections were prepared from annealed samples and studied using a TESCAN LYRA 3 XMU FEG/SEM×FIB scanning electron microscope (SEM) and a JEOL JSM6460 SEM with an Oxford Instruments energy dispersive X-ray (EDX) analyser.

Table I
Thermal treatment of the samples

Sample	T [°C]	t [min]	Regime
1	250	25	flash
2	300	25	flash
3	200	30	ramp
4	250	30	ramp
5	300	30	ramp
6	350	25	flash

The main emphasis was placed on the characterization of sintered Ag layers by means of nanoindentation experiments. Microhardness and other mechanical properties of sintered Ag layers were measured by instrumented indentation technique using a Fischerscope H100 depth sensing indentation tester equipped with Berkovich indenter.

3. Results and discussion

Fig. 1 shows TEM micrographs of Ag nanoparticles on a holey carbon film. The majority of particles have diameter below 10 nm (Fig. 1a), with a narrow size distribution. Only sporadic clusters of larger particles were found (Fig. 1b). Overall quality of this in-house prepared nanopowder was better and the particle size smaller than the one of the commercial nanopowder (Fig. 1c) and the one of the nanopowder prepared in our laboratory a year ago using a slightly different method of wet chemical analysis (Fig. 1d), both reported in our similar previous studies^{4,5}.

Fig. 2 shows SEM micrographs of cross sections of interfacial regions of a selected subset of studied samples. All samples showed well sintered Ag layers with a small volume fraction of pores. Only the microstructure of Ag layer annealed at the lowest temperature of 200 °C reveals signs of the original powder-like constitution of the layer (Fig. 2c). Furthermore, the characteristic size of fuzzy objects in Fig. 2c is substantially larger than the average nanoparticle size, meaning that we captured an intermediate stage of sintering with individual nanoparticles fully sin-

tered in compact clusters but the clusters incompletely sintered in the macroscopic bulk material.

An increasing thickness of interface layer was observed with increasing temperature of annealing. Series of EDX analyses across the interface detected high oxygen content, which corresponds to formation of Cu₂O interlayer. Comparing pairs of micrographs **a** vs. **d** and **b** vs. **e** in Fig. 2, it is seen that “flash” temperature setup produces (even in a slightly shorter time) more compact and homogeneous oxide layers with sharper interfaces and higher peak values of oxygen content.

The look of cross sections of sintered layers observed in the SEM does not reveal any substantial differences compared to previously studied materials after similar heat treatment^{4,5}. However the local mechanical testing of the layers turned out to be more conclusive. Results of depth sensing indentation tests are summarized in Table II. Each value is the average of at least 40 measurements. Martens hardness H_M , indentation hardness H_{IT} , elastic modulus $E_{IT}=E/(1-\nu^2)$, where E is Young’s modulus and ν is Poisson’s ratio, and creep CR values were obtained at testing load of 5 mN. The creep values after 5 s dwell time are expressed as the percentage of the maximum indentation depth.

The results show that the „flash“ annealing regime (samples 1 and 2) leads to slightly better mechanical properties than the „ramp“ annealing regime at the same temperatures (samples 4 and 5). An explanation of this difference may lie in the time dependence of the intensity of sintering proces. We suppose that during the slow heating

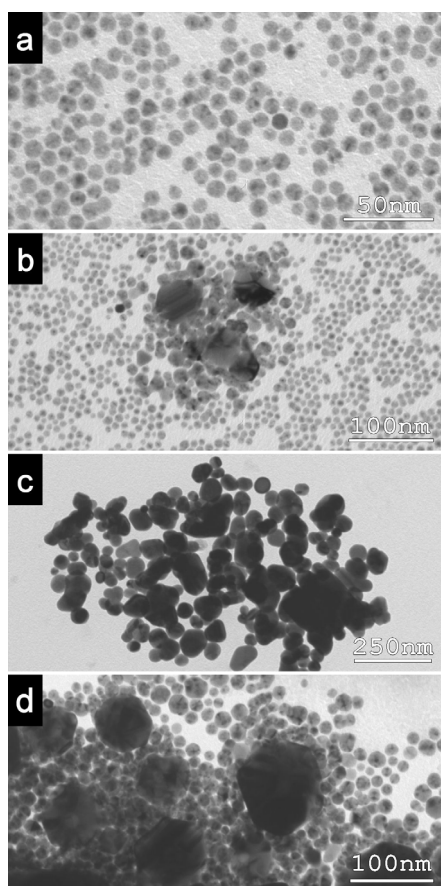


Fig. 1. TEM micrographs of in-house prepared Ag nanoparticles (a,b), a commercial product (c) and an older variant of in-house prepared Ag nanoparticles (d)

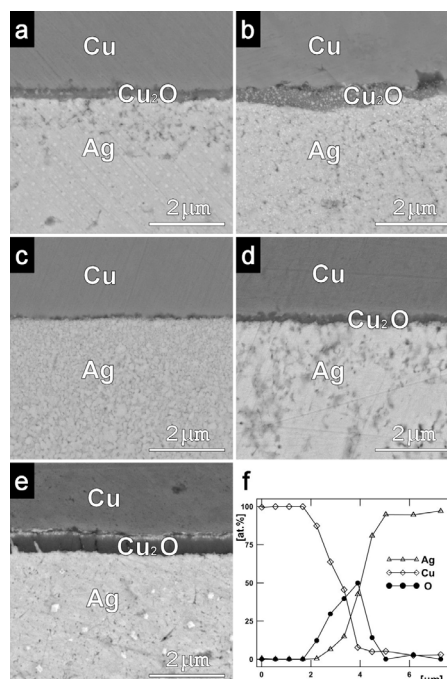


Fig. 2. SEM micrographs (signal of backscattered electrons) of Cu/Ag interface in samples 1 (a), 2 (b), 3 (c), 4 (d) and 5 (e), together with the results of EDX analyses across the interface in sample 5 (f)

Table II
Results of depth sensing indentation tests

Sample	HM [GPa]	H _{IT} [GPa]	E _{IT} [GPa]	CR [%]
1	0.90±0.10	1.15±0.07	20±2	3.3±0.9
2	1.08±0.25	1.82±0.15	37±3	1.3±0.4
3	0.72±0.12	1.10±0.25	17±4	4.2±1.5
4	0.87±0.14	1.20±0.18	18±4	3.5±1.2
5	1.00±0.46	1.43±0.44	32±4	3.0±1.1
6	0.85±0.06	1.07±0.09	35±2	3.0±1.0

up (the „ramp“ regime) individual nanoparticles at some temperature sinter to bigger clusters and in this stage they lose all the driving force for easy melting given by their small size. Further sintering of clusters is more difficult, resulting in pores (observed best in Fig. 2c) and worse mechanical properties.

The effect of annealing temperature is stronger than that of annealing regime. The values in Tab. II show a substantial improvement during the annealing temperature increase from 250 to 300 °C (samples 1 and 4 vs. samples 2 and 5). The results of indentation tests enabled us to settle the optimum thermal treatment. The mechanical parameters of samples 1, 2 and 6 treated in „flash“ regime showed less scatter than those of samples treated in „ramp“ regime. The highest hardness and elastic modulus [H_{IT}=(1.82±0.15) GPa and E_{IT}=(37±3) GPa] were achieved for sample treated at 300 °C in „flash“ regime.

The comparison of the values shown in Tab. II with the results obtained previously on sandwiches prepared using a commercial Ag nanopowder⁴ [H_{IT}=(0.6±0.2) GPa and E_{IT}=(35±15) GPa] shows much better mechanical properties of recently presented Ag layers. The results of indentation tests of sintered Ag layers of an in-house Ag nanopowder prepared previously by different procedure⁵ [H_{IT}=(1.25±0.5) GPa and E_{IT}=(35±7) GPa] showed a very large scatter of measured values because of the heterogeneous nanoAg grain size and sample porosity. The decrease in particle size to 10 nm and improvement in particle size uniformity led to well sintered nanoAg layers with low porosity. Consequently the scatter in mechanical parameters substantially decreased.

4. Summary

Mechanical properties of sintered layers of Ag nanopowder prepared in various annealing regimes were studied. Comparison between the in-house prepared Ag nanopowder and a commercial product shows smaller average particle size and more uniform particle size of the former. This leads to well sintered nanoAg layers with low porosity. Consequently the scatter in mechanical parameters substantially decreases. For Ag nanopowder the annealing temperature as low as 200 °C is sufficient to

produce a continuous Ag layer and to form a firm junction between copper plates. A Cu₂O transition layer of increasing thickness is observed at the Cu-Ag interfaces annealed at 200 to 350 °C. Mechanical properties of the sintered Ag nanopowder layer reflect obviously the choice of annealing temperature. Moreover also other details play important role, namely the heating rate. The results of indentation tests enabled us to settle the optimum thermal treatment. The highest hardness and elastic modulus [H_{IT}=(1.82±0.15) GPa and E_{IT}=(37±3) GPa] were achieved for sample treated at 300 °C in fast heating regime.

The financial support was provided by the Czech Science Foundation (Project 106/09/0700).

REFERENCES

- Dinsdale A., Watson A., Kroupa A., Vrestal J., Zemanova A., Vizdal J.: *COST Action 531 - Atlas of Phase Diagrams for Lead-Free Soldering*. COST office, Brno 2008.
- Pawlow P.: *Z. Phys. Chem.* 65, 545 (1909).
- Youn J. I., Ha W., Kim Y.: *J. Adv. Mater. Res.* 15-17, 995 (2007).
- Sopoušek J., Buršík J., Zálešák J., Buršíková V., Brož P.: *Science of Sintering* 43, 33 (2011).
- Buršík J., Sopoušek J., Buršíková V., Stýskalík A., Škoda D.: *Chem. Listy* 105, s777 (2011).

J. Buršík^a, V. Buršíková^{b,c}, Z. Pešina^d, and J. Sopoušek^e (^a*Institute of Physics of Materials, ASCR, Brno*, ^b*Masaryk University, Faculty of Science, Regional R&D center for low-cost plasma and nanotechnology surface modifications, Brno*, ^c*Masaryk University, CEITEC, Brno*, ^d*Brno University of Technology, Faculty of Mechanical Engineering, Brno*, ^e*Masaryk University, Faculty of Science, Department of Chemistry, Brno, Czech Republic*): **Mechanical Properties and Microstructure of Model Lead-Free Joints for Electronics Made with Use of Nanopowders**

Ag nanopowders were prepared as potential low-toxic constituents of novel solders by a chemical wet synthesis. Resulting nanoparticles were characterized using a transmission electron microscope. Model joints, i.e. sandwiches consisting of thin copper plates with Ag nanopowder interlayer were prepared and annealed at various temperatures. Metallographic cross-sections were studied using a scanning electron microscope. The main emphasis was placed on the characterization of sintered Ag layers on cross-sections by means of nanoindentation experiments. Microhardness and other mechanical properties of sintered Ag layers were measured by instrumented indentation with Berkovich indenter. Both the mechanical properties and the observed microstructure were compared with our previous results obtained on similar materials.

MICROSTRUCTURE AND PROPERTIES OF nc-WC/a-C COATING DEPOSITED ON HIGH SPEED STEEL BY MAGNETRON SPUTTERING

GRZEGORZ CEMPURA^a, TOMASZ MOSKALEWICZ^a, BOGDAN WENDLER^b, FRANTIŠEK LOFAJ^c, and ALEKSANDRA CZYRSKA-FILEMONOWICZ^a

^a AGH University of Science and Technology, Al. Mickiewicza 30, 30-059 Krakow, Poland, ^b Technical University of Łódź, ul. Stefanowskiego 1/15, 90-924 Łódź, Poland, ^c Institute of Materials Research of SAS, Watsonova 47, 040 01 Košice, Slovakia
cempura@agh.edu.pl

Keywords: microstructure, nc-WC/a-C coating, magnetron sputtering, nanocomposites, mechanical properties

1. Introduction

Coefficient of friction (COF) of engineering materials may be decreased by application of low-friction nanocomposite nc-WC/a-C coating^{1,2}.

The aim of the present investigation was a microstructure characterization as well as determination of selected micro-mechanical and tribological properties (COF, hardness, Young's modulus, coating's adhesion to the substrate) of the nc-WC/a-C coating deposited on high speed steel by magnetron sputtering.

2. Experimental details

Prior to the coating deposition, the HS6-5-2 high speed steel (chemical composition is given in Table I) was heat treated as follows: heating to 1150 °C with two 5 minutes' steps (at 550 °C and 850 °C), annealed at 1150 °C for 15 minutes and quenched in oil. In the last step steel was hold at 550 °C for one hour and cooled down with the furnace. The nc-WC/a-C coating was deposited by magnetron sputtering. The details of coating deposition are given in ref.³. An intermediate layer was deposited in order to improve the adhesion of the nanocomposite coating to steel substrate.

Microstructural investigation was carried out by light microscopy (LM), scanning- and analytical transmission electron microscopy (SEM, TEM). The SEM investigation was performed by Zeiss NEON 1540EsB microscope equipped in Quantax 200 X-ray Energy Dispersive Spectrometer of Bruker. The TEM investigation was performed by JEOL JEM-2010 ARP and FEI Tecnai G2 microscopes. Specimens for TEM were prepared as cross-section lamellas by Focused Ion Beam (FIB) technique using Zeiss NEON 1540EsB. Phase identification of the

coated steel was performed by Selected Area Electron Diffraction (SAED) technique and by X-Ray diffraction (XRD). XRD investigation was carried out using Siemens D500 diffractometer ($\lambda=1.54 \text{ \AA}$) on plan view specimens. The analysis of SAED patterns was supported by JEMS software⁴. Surface topography was studied with Atomic Force Microscope (AFM) Dimension 3000 of Digital Instruments (using Veeco SNL-10 indenters).

Adhesion of the coating to the substrate was measured by micro-scratch technique using Rockwell stylus. Scratch-tests were performed under increasing load (0.03–30 N) and scratch length of 3 mm. The COF of the substrate-coating system were measured on with a ball-on-disc apparatus using Al₂O₃ ball with diameter of 1 mm. Indentation hardness and reduced elastic modulus were determined with the CSM Micro Combi Tester (Vickers diamond indenter and load in the range of 10 mN–50 mN). Indentation data were analyzed by Oliver & Pharr method⁵, (9 indentation tests were performed).

3. Results and Discussion

Microstructure

Investigation of the coating's microstructure by SAED and XRD revealed a presence of the W₃C phase (cubic primitive, cp) within the coating. Ferrite and Fe₃W₃C (face centered cubic, fcc) were found in the steel substrate using Bragg-Brentano (B-B) and Grazing Incidence X-ray Diffraction (GIXRD), incidence angle $\alpha_p=5^\circ$. The thickness of the coating was measured on SEM micrographs (Fig. 1) as 1.8 μm .

The SEM-EDS investigation showed enrichment of tungsten in an intermediate layer. The TEM micrograph of the coating is presented in Fig. 2.

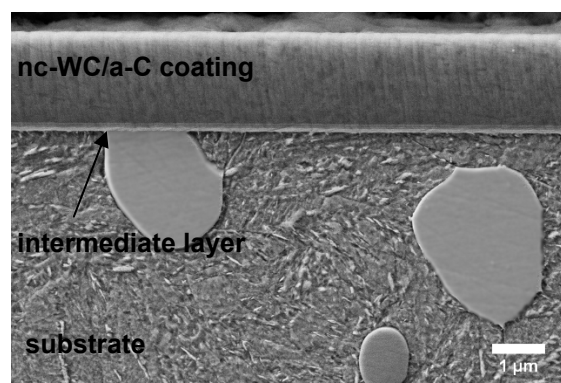


Fig. 1. Microstructure of nc-WC/a-C coating on HS6-5-2 steel, SEM - cross section

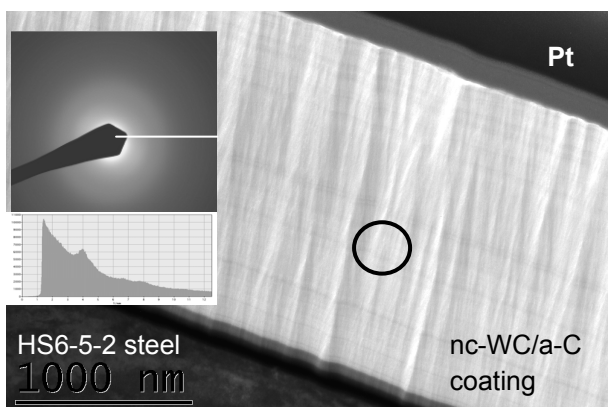


Fig. 2. Microstructure of nc-WC/a-C coating on HS6-5-2 steel and SAED pattern from marked area within the coating as well as intensity profile from marked line of SAED pattern

The SAED patterns from the coating area exhibited high blur of diffraction rings due to amorphous structure, however based on an intensity profile analysis it was possible to identify W_3C phase (a peak 111 ring is clearly visible).

The nc-WC/a-C coating had a columnar structure which was observed on FIB prepared lamellas as well as on cross section thin foils prepared by Precision Ion Polishing System (PIPS). HRTEM investigation of similar coating deposited on titanium alloy revealed that microstructure consisted of different nanocrystalline tungsten carbides (size of 2–5 nm) embedded in an amorphous matrix⁶.

The thickness of the intermediate layer present between the coating and substrate was measured on TEM foils as 50 nm.

The surface topography analysis was carried by AFM in areas of $50 \mu\text{m} \times 50 \mu\text{m}$. The results indicated high surface development: surface area factor, $\text{SAF}=1.0577$, root mean square $R_q=14.7 \text{ nm}$ and center line average height $R_a=10.5 \text{ nm}$.

Mechanical properties

Coating hardness measured at 10 mN and 50 mN loading was similar and equal to about 12.5 GPa, reduced Young modulus was about 199 GPa.

The investigated coating had a relatively good adhesion to the substrate. First cohesive cracks appeared at relatively low load of 4 N during scratch test. However the adhesive cracks were formed at load of 24 N. It was found that the nanocomposite nc-WC/aC coating significantly decreased COF from 0.7 for an uncoated steel to 0.1 for the coated one.

4. Summary

The nc-WC/a-C coating was deposited on HS-6-5-2 high speed steel by magnetron sputtering. Thickness of the coating was measured as $1.8 \mu\text{m}$. The coating consisted of nanocrystalline W_3C carbides embedded in an amorphous C matrix. The coating had a good adhesion to the steel substrate. The coating decreases COF and improves wear resistance properties of the steel.

The authors acknowledge financial support from the National Centre for Research and Development (NCBiR) under MNT ERA-NET HANCOC project (no 402/ERA-NET/2009).

REFERENCES

1. Carvalho N. J. M., DeHosson J. Th. M.: *Thin Solid Films* 150-159, 388 (2001).
2. Liu Y., Erdemir A., Meleti E. I.: *Surf. Coat. Technol.* 48-56, 82 (1996).
3. Wendler B. G., Pawlak W.: *J. Ach. Mater. Manuf. Eng.* 26, 207 (2008).
4. Stadelmann P.: *JEMS: Java Electron Microscopy Software*, Available from: <http://cime.epfl.ch/>.
5. Oliver W. C., Pharr G. M.: *J. Mater. Res.* 7, 1564 (1992).
6. Moskalewicz T., Wendler B., Czyska-Filemonowicz A.: *Mater. Char.* 61, 959 (2010).

G. Cempura^a, T. Moskalewicz^a, B. Wendler^b, F. Lofaj^c, and A. Czyska-Filemonowicz^a (^a AGH University of Science and Technology, Krakow, Poland, ^b Technical University of Łódź, Poland, ^c Institute of Materials Research of SAS, Košice, Slovakia): **Microstructure and Properties of nc-WC/a-C Coating Deposited on High Speed Steel by Magnetron Sputtering**

One possibility to improve friction properties of steel is deposition of nanocomposite coating. In this work the nanocomposite nc-WC/a-C coating was deposited on high speed H6-5-2 steel by magnetron sputtering. Microstructure investigation of the coating and the substrate were performed by means of scanning- and transmission electron microscopy (SEM, TEM) as well as X-ray diffractometry (XRD). It was found that the coating, $1.8 \mu\text{m}$ thick, was consisted of the W_3C phase (cubic primitive) embedded in an amorphous matrix. Selected properties (coating adhesion to the underlying substrate, reduced Young modulus, microhardness, coefficient of friction and wear resistance) were determined. The hardness of the coating was much higher than steel hardness. The nc-WC/a-C coated steel exhibited and lower coefficient of friction than the uncoated steel.

EFFECT OF DEPOSITION CONDITIONS ON MECHANICAL PROPERTIES OF MAGNETRON SPUTTERED SiC THIN FILMS

RADIM ČTVRTLÍK^a, VALERIY KULIKOVSKY^b, PETR BOHÁČ^b, and OLGA BLÁHOVÁ^c

^a Palacky University, Faculty of Science, Regional Centre of Advanced Technologies and Materials, Joint Laboratory of Optics of Palacky University and Institute of Physics of Academy of Sciences of the Czech Republic, 17. listopadu 50A, 779 00 Olomouc, ^b Institute of Physics, Academy of Sciences of the Czech Republic, v.v.i., Na Slovance 2, 182 21 Praha, ^c New Technologies-Research Centre, University of West Bohemia, Univerzitní 8, 306 14 Plzeň, Czech Republic
ctvrtlik@fzu.cz

Keywords: silicon carbide, thin films, nanoindentation, mechanical properties, coefficient of friction

1. Introduction

Silicon carbide (SiC) is a promising material for a variety of mechanical and high temperature applications as well as for use in microelectromechanical systems (MEMS) due to its excellent physical, chemical and mechanical properties.

SiC films and coatings are one of the most commonly used forms of SiC as a functional material, especially due to low costs and relatively simple preparation.

Amorphous hydrogen-free silicon carbide coatings (a-SiC) exhibit a variety of attractive properties, such as high hardness and wear resistance, low intrinsic stress, good thermal stability and adhesion to steel substrates. Furthermore, their high hardness can be reached by performing deposition at room temperature that is technologically beneficial. On the other hand, they possess high coefficient of friction, especially in comparison with carbon-based coatings^{1–3}.

Various practical applications of thin films and coatings require specific combinations of their mechanical properties like hardness, toughness, wear resistance, coefficient of friction and others that can often be hardly compatible. In this respect the interrelationship between deposition conditions, composition, structure and mechanical properties is a key issue.

The aim of this paper is to outline how the deposition conditions of DC magnetron sputtering affect mechanical properties (hardness, modulus of elasticity and coefficient of friction) of amorphous and nanocrystalline SiC thin films and how to prepare SiC films with specific combinations of mechanical and tribological properties. The first

part deals with the effect of substrate bias and temperature whilst the second part with carbon concentration. The hardness of the films is also compared with the corresponding single crystal.

2. Experimental details

Amorphous and nanocrystalline SiC films were deposited by DC magnetron sputtering using the Leybold-Heraeus Z 550M sputtering plant. The target-substrate distance was 50 mm and the discharge power was typically 300 W. All the films were prepared on the Si(111) substrates except the films for tribological tests that were deposited on steel substrates.

In the first case DC sputtering of hot pressed conductive SiC_{1.1} target in argon at pressure of 0.5 Pa was used. Hydrogen-free a-SiC films were deposited on grounded or biased substrates. A bias voltage ranging from 0 to –160 V was applied at deposition to unheated substrates using 13.56 MHz power source. Some films were deposited on substrates preheated to temperatures of 200, 400, 600 and 750 °C.

In the second case amorphous hydrogenated silicon carbide films (a-SiC:H) were sputtered from SiC_{1.1} target in the gas mixture of argon and CH₄. Flow rate of CH₄ was changed from 0 to 12 sccm in order to prepare films with various carbon concentrations, corresponding CH₄/Ar ratio varied in the range of 0–48 %. Bias voltage of –55 V was applied on the unheated substrates.

The film structure was studied by micro-Raman spectroscopy. Composition was investigated using electron probe X-ray microanalysis (EPMA). Internal stress was estimated according to the Stoney's classical formula⁴.

Nanoindentation was performed using the Nano-TestTM NTX system in a load controlled mode with a calibrated Berkovich tip. Indentation Hardness and reduced modulus were determined from nanoindentation curves using the analysis by Oliver and Pharr⁵. The peak load of 20 mN was chosen in order to ensure fully plasticity and minimize the influence of surface roughness and other effects related to the shallow indents, whilst ensuring that the maximum depth did not exceed ~13 % of the film thickness. So the presented hardness and elastic modulus values can be considered as film-dominated. The average values of hardness and reduced elastic modulus were calculated from 5 independent measurements. The reduced indentation modulus E_r that takes into account also the elastic deformation of the indenter is defined as

$$\frac{1}{E_r} = \frac{1-\nu^2}{E} + \frac{1-\nu_i^2}{E_i} \quad (1)$$

where E and ν , and $E_i = 1141$ GPa and $\nu_i = 0.07$, describe

the elastic modulus and Poisson's ratio of the sample and the indenter, respectively.

Pin-on-disc tribometer with alumina ball with diameter of 6 mm was used for investigation of coefficient of friction. Samples were tested at normal load of 5 N and sliding velocity of 1 cm s⁻¹ for a sliding radius of 5 mm. Each test consisted of 2000 cycles.

3. Results and discussion

3.1. Hydrogen-free amorphous SiC films

Thickness of the hydrogen-free SiC films deposited in pure argon varied in dependence on deposition conditions in the range of 3.2–4.4 μm. The carbon concentration changed only slightly with the changing substrate bias or temperature and was approx. 52 at.% for all of the films. That means that the change of mechanical properties is linked with the change of the film structure.

Raman spectroscopy pointed out that all of the investigated films are amorphous except the film deposited at 750 °C, where traces of crystalline phase were revealed.

Indentation hardness and reduced modulus of a-SiC films deposited on unheated substrates as a function of negative substrate bias are shown in Fig. 1. As can be seen hardness and reduced modulus decrease with increasing bias voltage. Compressive stress of these films initially increases to 1.4 GPa along with increasing bias voltage up to -100 V and then decreases.

These effects are connected with the creation of numerous point defects and reduction of the short-range order and strength of interatomic bonding due to the ion bombardment. The influence of increasing Ar concentration in the films is also probably involved⁶.

Increase of substrate temperature during deposition results in gradual increase of indentation hardness as well as reduced modulus as can be seen from Fig. 2. This positive correlation between hardness and modulus is well known for hard coatings and has been frequently reported in the literature^{7,8}. Increase of deposition temperature

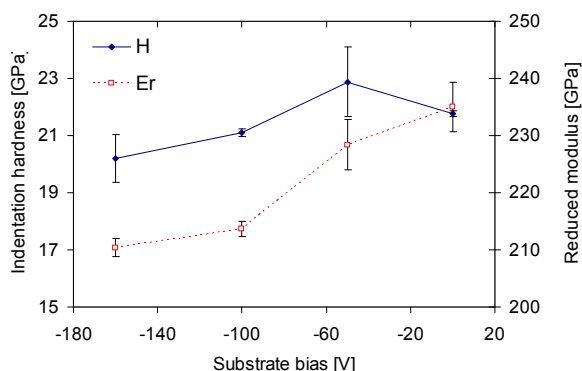


Fig. 1. Indentation hardness and reduced modulus of SiC films as a function of substrate bias

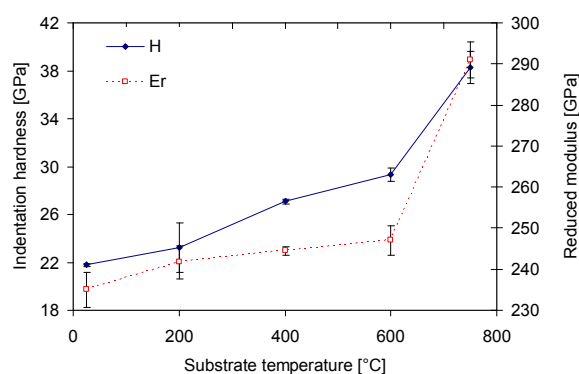


Fig. 2. Indentation hardness and reduced modulus of SiC films as a function of substrate temperature

simultaneously leads to the monotonous decrease of compressive stress in the films and improvement of the atomic short-range order and the bonding between the clusters⁹. It should be noted that the film deposited at 750 °C, where the partial crystallization of SiC takes place inside the amorphous matrix, possesses hardness of 40 GPa that is significantly higher in comparison with approx. 36 GPa of α-SiC(001). The details are given in ref.¹⁰.

3.2. Hydrogenated amorphous SiC films

Although the amorphous Si₄₈C₅₂ films possess high hardness, they also exhibit very high coefficient of friction of approx. 0.7.

It is well known that for good tribological performance the weak bonding between contacting surfaces and low surface roughness are required. In the case of amorphous carbon based films the former is fulfilled due to the layered structure with weak van der Waals bonding between layers⁹. The surface roughness of amorphous films is generally lower than for crystalline ones.

The a-SiC films with various excess of carbon were deposited by adding CH₄ to Ar during deposition at bias voltage of -55 V in order to investigate the possibilities of reduction of coefficient friction. Such approach allowed to limit a content of hydrogen in the films in comparison to other deposition methods¹¹.

Fig. 3 describes the indentation hardness and reduced modulus of a-SiC:H films with thickness of 1.9–2.5 μm as a function of carbon concentration. As the carbon content increases from 52 at.% to 92 at.% the hardness and modulus decreases from 23 to 10 GPa and from 222 to 97 GPa, respectively. Increase of carbon concentration also leads to reduction of compressive stress from 1.1 to 0.3 GPa. It is a result of atomic bonds termination by hydrogen that decreases the number of eventual cross-links in the atomic network⁹.

The hydrogen concentration in the investigated films was estimated from the analysis of the Raman spectra using empirical relation originally presented for hydrogenated amorphous carbon¹². It revealed that hydrogen

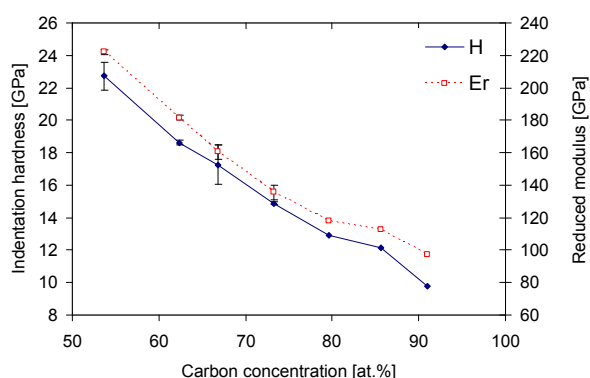


Fig. 3. Indentation hardness and reduced modulus of a-SiC:H films as a function of carbon concentration

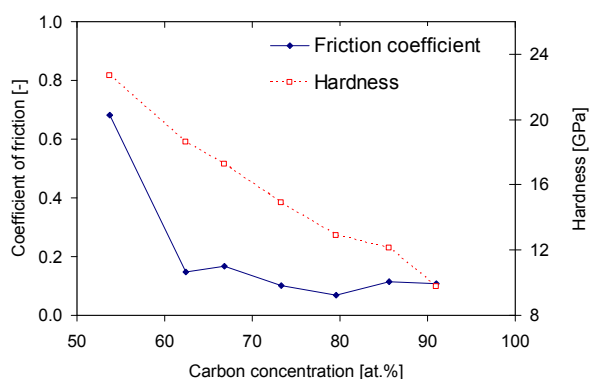


Fig. 4. Coefficient of friction and indentation hardness of a-SiC:H films as a function of carbon concentration

concentration is approx. 26–28 at.% for the films with carbon concentration above 67 at.%, i.e. for films deposited at higher CH₄ flow rates.

Results of Pin-on-disc experiments are summarized in Fig. 4. One can see an initial dramatic decrease of coefficient of friction from 0.7 to 0.15 with increase of carbon concentration in the films from 52 to 62 at.%. Further increase of carbon content results only in moderate reduction of friction coefficient. This decrease of friction is probably connected with the raising number of a-C:H clusters and passivation of dangling bonds in the a-SiC:H clusters by hydrogen or its radical groups.

4. Conclusion

The paper demonstrated how appropriate choice of deposition parameters (substrate bias and temperature) can lead to the production of a-SiC films with various mechanical or tribological properties.

It has been presented that indentation hardness and reduced modulus of hydrogen-free a-SiC decrease with increasing bias voltage, whilst they grow with increasing temperature.

First traces of crystallization were observed for the film sputtered at 750 °C with hardness of 40 GPa. Such high hardness exceeding the a-SiC single-crystal is linked to the nanocrystalline structure of the film.

Friction coefficient of a-SiC:H films was optimized by changing the carbon concentration. The film deposited in pure Ar (52 at.% of C) exhibits value of 0.7. Increase of carbon concentration leads to gradual decrease of hardness in the whole range from 52 to 91 at.%, whilst friction coefficient drops dramatically already at small addition of excess carbon (62 at.%) and then decrease slightly.

Thus using appropriate deposition conditions it is possible to prepare a-SiC:H films with sufficiently high hardness of approx. 19 GPa and a low coefficient of friction of approx. 0.15.

This work has been supported by the Operational Program Research and Development for Innovations - European Regional Development Fund (CZ.1.05/2.1.00/03.0058) and co-financed from the Operational Program Education for Competitiveness - European Social Fund (project CZ.1.07/2.3.00/20.0017) of the Ministry of Education, Youth and Sports of the Czech Republic and by the Technology Agency of the Czech Republic (TA01010517).

REFERENCES

- Kulikovskiy V., Vorliček V., Bohac P., Kurdyumov A., Jastrabik L.: *Diamond Relat. Mater.* 13, 1350 (2004).
- Ctvrtilik R., Stranyanek M., Bohac P., Kulikovskiy V., Suchanek J.: *Int. J. Mater. Res.* 8, 871 (2008).
- Sobota J., Grossman J., Vyskočil J., Novák R., Fořt T., Vítů T., Dupák L.: *Chem. Listy* 104, 375 (2010).
- Stoney G. G.: *Proc. R. Soc. London A* 82, 172 (1909).
- Oliver W. C., Pharr G. M.: *J. Mat. Res.* 7, 1564 (1992).
- Ohring M., v knize: *Materials Science of Thin Films. 2nd. ed.*, Academic Press, London 2002.
- Han Z. H., Li G. Y.: *Mater. Lett.* 57, 899 (2002).
- Jacobsohn L. G., Nastasi M.: *Surf. Coat. Technol.* 200, 1472 (2005).
- Kulikovskiy V., Vorliceck V., Ctvrtilik R., Bohac P., Suchanek J., Blahova O., Jastrabik L.: *Surf. Coat. Technol.* 205, 3372 (2011).
- Kulikovskiy V., Vorliceck V., Bohac P., Stranyanek M., Ctvrtilik R., Kurdyumov A., Jastrabik L.: *Surf. Coat. Technol.* 202, 1738 (2008).
- Precht W., Czyniewski A.: *Surf. Coat. Technol.* 174–175, 979 (2003).
- Casiraghi C., Ferrari A. C., Robertson J.: *Phys. Rev. B* 72, 085401 (2005).

R. Čtvrtlík^a, V. Kulikovský^b, P. Boháč^b, and O. Bláhová^c (^a*Palacky University, Faculty of Science, Regional Centre of Advanced Technologies and Materials, Joint Laboratory of Optics of Palacky University and Institute of Physics of Academy of Sciences of the Czech Republic, Olomouc,* ^b*Institute of Physics, Academy of Sciences of the Czech Republic, Praha,* ^c*New Technologies-Research Centre, University of West Bohemia, Plzeň, Czech Republic*): **Effect of Deposition Conditions on Mechanical Properties of Magnetron Sputtered SiC Thin Films**

The interdependence of mechanical properties (hardness, elastic modulus, internal stress, coefficient of friction), structure and composition of various amorphous and nanocrystalline DC magnetron and DC reactive magnetron sputtered SiC and SiC:H films was studied.

Composition was determined by electron microanalyses and structure was investigated using Raman spectroscopy. Indentation hardness and reduced modulus were measured by instrumented nanoindentation, the coefficient of friction was evaluated using pin-on-disc method.

It has been shown that mechanical and tribological properties of a-SiC are strongly influenced by conditions of deposition process. Using appropriate deposition setup it is possible to obtain superhard nanocrystalline films with hardness of 40 GPa (higher than α -SiC) as well as films compromising high hardness (approx. 19 GPa) and relatively low friction (approx. 0.15).

ANALYSIS OF CROSS-SECTION SURFACE ROUGHNESS EVOLUTION OF CARBON FIBRE REINFORCED POLYMER UNDER FATIGUE LOADING

TOMÁŠ DOKTOR^a, JAROSLAV VALACH^b,
DANIEL KYTÝŘ^b, TOMÁŠ FÍLA^b,
JÍŘÍ MINSTER^b, and MICHAELA
KOSTELECKÁ^c

^a Czech Technical University in Prague, Faculty of Transportation Sciences, Department of Mechanics and Materials, Na Florenci 25, 110 00 Prague 1, ^b Academy of Sciences of the Czech Republic, Institute of Theoretical and Applied Mechanics v.v.i., Prosecká 76, 190 00, Prague 9, ^c Czech Technical University in Prague, Klokner Institute, Šolínova 7, 166 08, Prague 6, Czech republic
xdoktor@fd.cvut.cz

Keywords: surface roughness, degradation monitoring, SEM, LSCM

1. Introduction

The article deals with monitoring of degradation of fibre reinforced thermoplastic matrix composite under cyclic loading. The investigated material is composed of polyphenylsulfid matrix and carbon fibres arranged symmetrically in 8 plies with three different fibre orientation (0, 45 and 90 degrees). The material is widely used for secondary, i.e. non-structural elements in aircraft industry. The main aim of the presented work is to correlate observed microstructural changes to measurable morphometric properties and the number of applied load cycles.

2. Materials and methods

Fatigue loading

Four specimens of carbon fibre reinforced polymer¹ (CFRP) were subjected to cyclic loading. The investigated specimens were prismatic, with rectangular cross section (dimensions 12.5×2.5 mm) and length 125 mm. The dimensions were chosen due to limited dimensions of working chambers of used microscopes. The cyclic loading was carried out using loading device Instron 1293 (Instron, Nordwood, US) in three-point bending arrangement^{2,3}. For the cyclic loading sinusoidal run of the loading force was used. The upper limit of deflection was 5 mm. Frequency 5 Hz was chosen for the cyclic loading to avoid heat accumulation^{4,5} in the tested specimens. After selected numbers of loading cycles the surface of the specimens was observed by scanning electron microscope (SEM) and laser scanning confocal microscope (LSCM).

Surface analysis

Using confocal microscope LEXT OLS 3000 (Olympus Corporation, Tokyo, Japan) surface profile was scanned and images (dimensions 2250×9150 μm) were obtained (1 px in the images corresponds to 9 μm). Information about the surface was obtained in form of two-dimensional matrix containing ascertained heights. Each image was divided into several regions of interest⁶ (dimensions 500×500 μm) and in these regions roughness characteristics were estimated (described in detail by Dudíková⁷).

A scanning electron microscope MIRA LMU (TESCAN, a.s., Brno, Czech Republic) was used for observation of degradation processes on the surface of investigated specimens. The images were acquired in high vacuum mode using secondary electron detector. Images with magnification 1000× were used to assess of changes on the samples' surface.

3. Results

Roughness evolution

Surface characteristics were estimated in 4 states during the test process. Evolution of the average roughness is depicted in Fig. 1 and in Fig. 2. Increasing indicators of the surface roughness were observed with increasing number of loading cycles.

SEM inspection

SEM was employed to observe changes on the specimens' surface. Free edge of the specimen in four steps of the fatigue loading is depicted in Fig. 3. The images were acquired with magnification 1000× (white bars correspond to 100 μm).

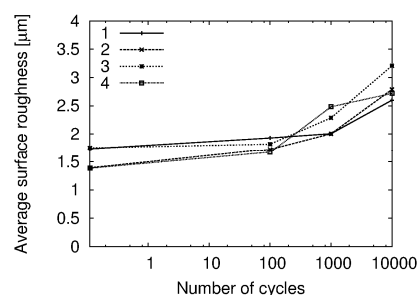


Fig. 1. Average surface roughness (R_a)

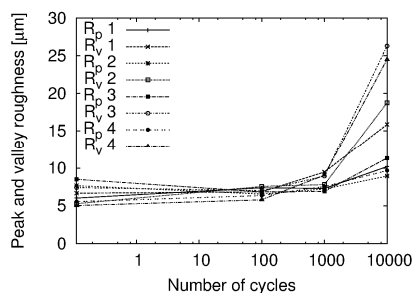


Fig. 2. Peak and valley roughness (R_p , R_v)

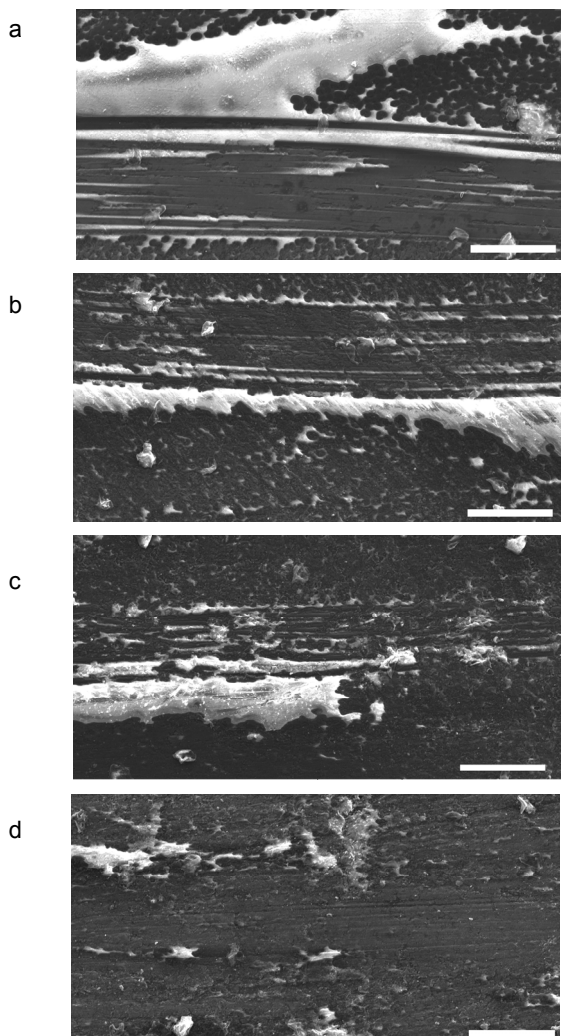


Fig. 3. Free edge of specimen: intact (a) and 10^2 (b), 10^3 (c) and 10^4 (d) cycles

4. Conclusions

In this preliminary analysis degradation monitoring of CFRP composite using surface roughness measurements was performed. The increase of surface roughness observed with increasing number of loading cycles indicates at the level of micromechanics changes in fibre-matrix interface and also changes in the matrix structure itself. Increasing values of R_p are connected with detachment of matrix from the fibers and increasing values of R_v show degradation of the matrix. Obtained results of surface analysis correspond with result of SEM inspection performed after distinct steps of the fatigue loading. The SEM images show decreasing surface quality with higher number of loading cycles (both in detachment of fibres and changes in the matrix).

The research has been supported by Grant Agency of the Czech Technical University in Prague (grants No. SGS12/205/OHK2/3T/16 and SGS10/227/OHK1/2T/31), research plan of the Academy of Sciences of the Czech republic AV0Z0710524 and research plan of the Ministry of Education, Youth and Sports MSM6840770043.

REFERENCES

1. Airbus: *AIMS – Airbus Material Specification*, Airbus S.A.S (2007).
2. De Baere, I. et al.: *Int. J. Fatigue* 31, 1095 (2006).
3. Van Paeppegem W., et al.: *Int. J. Fatigue* 72, 212 (2006).
4. Steinberger R., et al.: *Int. J. Fatigue* 28, 1340 (2006).
5. Toubal L.: *Int. J. Fatigue* 28, 1867 (2006).
6. Al-Shammery H. D. O., et al.: *Dent. Mater.* 23, 736 (2007).
7. Dudíková M., et al.: *Chem. Listy* 105, s790 (2011).

T. Doktor^a, J. Valach^b, D. Kytýř^b, T. Fíla^b, J. Minster^b, and M. Kostecká^c (^a Czech Technical University in Prague, Faculty of Transportation Sciences, Department of Mechanics and Materials ^b Academy of Sciences of the Czech Republic, Institute of Theoretical and Applied Mechanics v.v.i., ^c Czech Technical University in Prague, Klokner Institute): **Analysis of Cross-Section Surface Roughness Evolution of Carbon Fibre Reinforced Polymer under Fatigue Loading**

The article deals with monitoring of degradation of carbon fibre reinforced polymer (CFRP) under cyclic loading. The investigated material is composed of polyphenylsulfid matrix and carbon fibres. Four specimens were subjected to repeated cyclic loading. During the fatigue loading surface of tested specimens was observed by scanning electron microscopy (SEM) and laser scanning confocal microscopy (LSCM) to obtain surface roughness characteristics and micrographs of surface morphology. With increasing number of cycles the measured surface characteristics showed increasing surface roughness indicating at the level of micromechanics detachment of matrix from the fibers and also changes in the matrix structure itself.

PREDICTION OF LOCAL LIMIT DEFORMATIONS OF STEEL SHEETS DEPENDING ON DEFORMATION SCHEME

EMIL EVIN, MIROSLAV TOMÁŠ,
and JOZEF VÝBOCH

Department of Technologies and Materials,
Faculty of Mechanical Engineering, Technical University
of Kosice, Mäsiarska 74, 040 01 Košice, Slovak Republic
Emil.Evin@tuke.sk
Miroslav.Tomas@tuke.sk

Keywords: local limit deformation, stress-strain state,
forming limit diagram, CCD camera, FEM simulation

1. Introduction

Regarding economic and ecological requests the main appeal for design, material science and production technology engineers is car's body parts weight decreasing. Car's body components design strategies are fixed to optimisation of material selection from aspects of both weight minimisation at first and preservation or improvement of functional properties (safety, power, fuel consumption, comfort, etc.)^{1–3}. ULSAB studies show weight decreasing potential of steel sheets components consists in lower thickness steel sheets application with higher strength properties and combined laser welded tailored blanks from these steel sheets (Table I).

Application of steel sheets with lower thickness and higher strength properties leads to technological characteristics of formability downgrading. Formability, or reached deformation degree (limit value) in sheet plane, respectively necking of cup wall thickness depends on material properties, stress-strain state, initial blank thickness and strain rate – Fig. 1 (ref.^{1,2,4}).

Stress state in sheet plane can be expressed by main stresses ratio $\alpha = \sigma_2/\sigma_1$ and strain state by main deformations ratio $\beta = \varepsilon_2/\varepsilon_1$ (Fig. 2), where first main (major) deformation $\varepsilon_1 > 0$, second main (minor) deformation $\varepsilon_2 < 0$ or $\varepsilon_2 > 0$.

Table I

Comparison of car's body parameters produced from different steel sheets

	Weight [kg]	Torsional stiffness [°/Nm]
Car's body based on typical high strength steels	300	>15 000
ULSAB	210	> 19 000
Car's body skeleton based on austenitic steel sheets	160	> 25 000

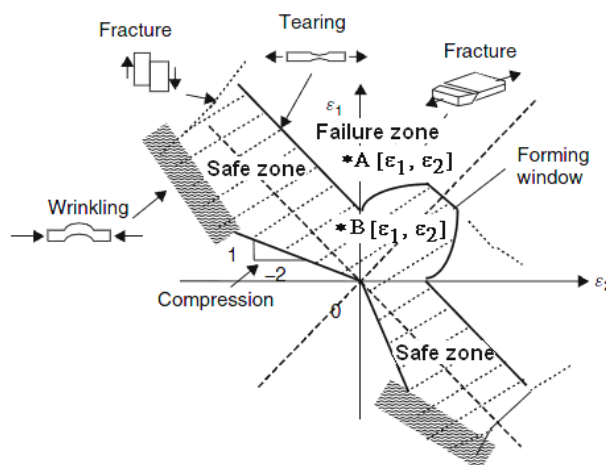


Fig. 1. Sheets formability window⁴

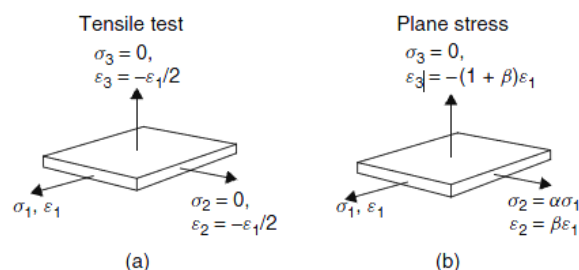


Fig. 2. Stress-strain states at stamping

At certain combination of major and minor deformations ε_1 and ε_2 in sheet plane localised deformation in critical area occurs, i.e. local narrow area occurs (neck), followed by fracture. Level of combination of major and minor deformations in sheet plane before localised deformation (before local narrowing) creates limit between good drawn parts – B point and failure drawn parts – A point. This dependence of limit deformations ε_{1c} and ε_{2c} in sheet plane is known as Keeler-Goodwin forming limiting diagram – FLD. Nowadays forming limiting curves (FLC) are considered as inseparable formability characteristic of steel sheets, because they quote development of deformation depending on time and also allows identifying deformation mechanism depending on strain state.

Position of FLC curve in FLD diagram depends not only on material properties, stress-strain state, but also on initial blank thickness, strain rate and friction between blank-die contact surfaces. As it is shown in Fig. 1, maxi-

mal major deformation ε_{1c} is located at areas near to $\varepsilon_{1c} = \pm \varepsilon_2$. When $\varepsilon_{1c} = -\varepsilon_2$ wrinkling occurs at pressings production. At crash situations wrinkling occurs first followed by fracture after overloading of limit fracture deformation. The lowest values of major deformation ε_{1c} are reached in areas where minor deformation $\varepsilon_2 = 0$. In area from $\varepsilon_{1c} = -2\varepsilon_2$ to $\varepsilon_{1c} = \varepsilon_2$ fracture occurs after local necking due to tensile stresses acting.

2. Methods of experimental research

Within last 50 years there was a lot of experimental work done and big effort invested in analytic and experimental creation of forming limit curves^{1,2,5,6}. In this contribution there are presented results of limit deformation research by application CCD video camera recording and by numerical simulation.

As experimental materials were used austenitic stainless steel sheet DIN 1.4301 and deep drawing quality steel sheet DX54D. Their chemical composition and mechanical properties are shown in Table II and Table III.

Localised plastic deformations were researched at deformation states within interval $\beta = (-1/2; 0)$. Deformation schemes were modelled on tensile test specimens with different notch radii – R5, R10, R17.5 and R25. Local limit deformations at experiments were researched using circle deformation grid ($l_0 = 2$ mm) etched on test specimens.

Testing machine TiraTEST 2300 was used and load velocity was set to 10 mm/min. Change of specimen's dimensions and grid's shape in notch area was continuously recorded by CCD camera. Local limit deformations $\varepsilon_1 = l_1/l_0$, $\varepsilon_2 = l_2/l_0$ were calculated and evaluated by software Matlab's Image Processing Toolbox^{1,5}. Used video-recording method also allows research all deformation history from test start to specimen fracture.

Deformation net dimensions were evaluated before

Table II
Chemical composition of experimental materials [%]

Material	C	Mn	Si	P	S	Al	N
DX54D	0.05	0.2	0.02	0.009	0.01	0.049	0.006
DIN 1.4301	0.07	2.0	1.0	0.045	0.03	Cr 19	Ni 10

Table III
Mechanical properties in 90° of rolling direction

Material	0.2% YS [MPa]	UTS [MPa]	K [MPa]	n_{90} [-]	r_{90} [-]
DX54D	184	311	487	0.215	1.59
DIN 1.4301	273	621	1491	0.515	0.99

deformation (initial state), before crack occurred (limit state) and after crack occurred (specimen fracture) – see Fig. 3. Following assumptions were considered to define limit state of deformations based on deformation history:

- homogeneous deformation occurs in the first phase, deformation history is linear $\varepsilon_{1i} = \beta_i \cdot (-\varepsilon_{2i}) \cap \beta_{i-1} \approx \beta_i$,
- localised deformation (diffuse necking) occurs at the second phase under constant loading, deformation history isn't linear $\varepsilon_{1i} = \beta_i \cdot (-\varepsilon_{2i}) \cap \beta_{n-2} > \beta_{1n-1}$,
- at the third phase localised neck (local necking) occurs of width $2 \cdot a_0$ and sudden drop of loading force is recorded, followed by fracture, where $\varepsilon_{1n-1} < \varepsilon_{1n} \cap \varepsilon_{2n-1} = \varepsilon_{2n} \cap \beta_{n-1} \approx \beta_n$.

Deformations evaluated from net dimensions at the

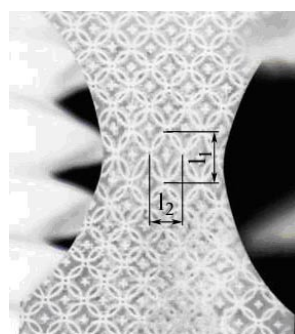


Fig. 3a. Etched deformation net before specimen cracking

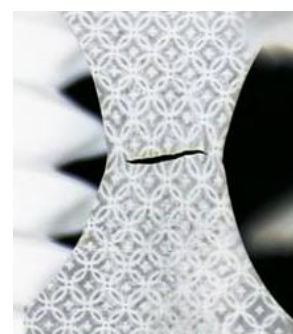


Fig. 3b. Deformation net after specimen cracking

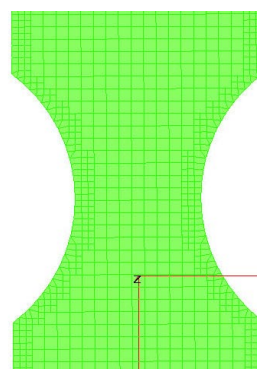


Fig. 4a. Meshed specimen in numerical simulation

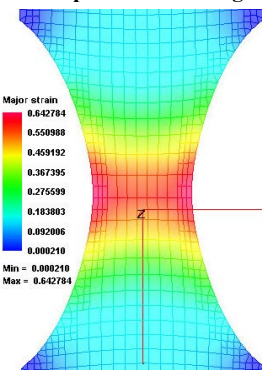


Fig. 4b. Limit state of major strain in numerical simulation

end of the second phase were defined as limit deformations; deformations evaluated in the third phase aren't useful for application at stamping processes, because fracture occurs – Fig. 3b.

Numerical simulation of necked specimens was done using Pam Stamp 2G simulation software. Specimen's models were defined and simulation set-up was done in pre-processing.

Specimen's models were created using 3D CAD/CAM software Pro/Engineer and exported into simulation software in neutral format igs. In Pam Stamp 2G meshing module specimens were meshed to square finite elements with dimension 2 mm – Fig. 4a. Following input data were

set up in Pam Stamp 2G preprocessor:

- basic material data (density, Young's modulus, Poisson's constant,
- blank thickness,
- strain-hardening curve defined by Hollomon's law according to data shown in Table III,
- Lankford's coefficients in directions 0°, 45° and 90° to rolling direction, as definition of sheet normal anisotropy,

- rolling direction 0° in longitudinal axis of specimens,
- Yield law defined by Hill 48 model.^{1,7}

Visualisation of computed data (post processing) allows displaying major σ_1 and minor σ_2 stress distribution, major ϵ_1 and minor ϵ_2 strain distribution, wall thickening, variation of forces, deformation energy etc. Localised deformation was researched in postprocessor by visualisation

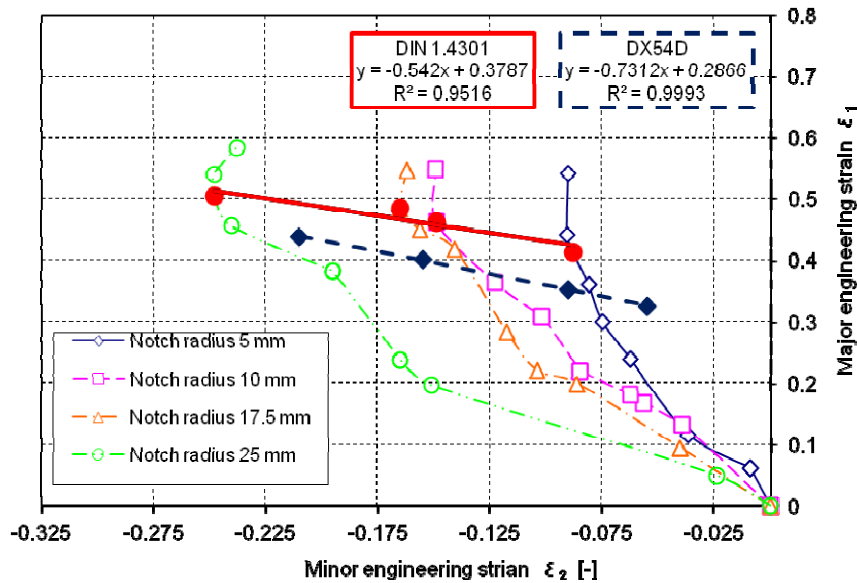


Fig. 5. Experimentally acquired forming limit curves

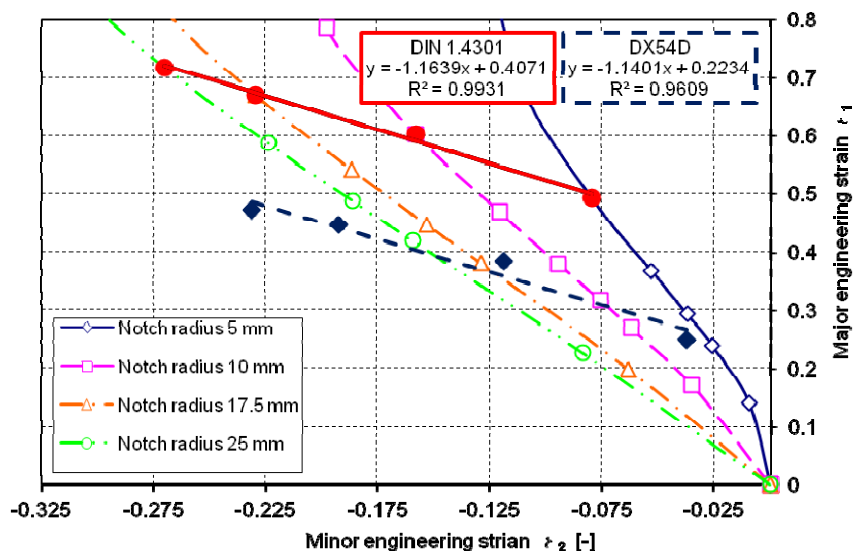


Fig. 6. Forming limit curves acquired from numerical simulation

of major ε_1 and minor ε_2 engineering deformations – Fig. 4b. Fig. 5 shows deformation paths of selected deformation net element with computed limit forming limit curves FLC for both materials.

A comparison of Fig. 5 and Fig. 6 shows there is good agreement between experimentally measured FLC and FLC computed by numerical simulation.

3. Reached results and discussion

The measured results of plastic deformation distribution from tensile test of necked specimens shows the deformation history is linear to the limit values described by FLC (Fig. 5). To define the limit formability conditions are important limit deformations in the sheet plane or limit values of material thinning before the plastic deformation localization – neck creation. If we put a curve through the points where there is a significant change of line slope (the critical value of deformation), we get the left part of the FLC. Comparing the FLC defined for austenitic steel sheet (material DIN 1.4301 – Fig. 5) and ferrite steel sheet (material DX54D) the FLC is situated higher the higher values of elongation and strain hardening exponent are. The values of these material characteristics are in the austenitic steel sheets larger than the values in low carbon steel sheets – material DX54D / Table II. The measured results show that the position of the FLC isn't affected by normal anisotropy ratio (austenitic steel sheet $r = 1$, low carbon steel sheet $r = 1.8$). Reached FLC comply with present knowledge^{1,8,9}. The finding that the position of FLC depends largely on the elongation and strain hardening exponent confirmed the results obtained with strain rate $\dot{\varphi} = 0.0083 \text{ s}^{-1}$. When changing the strain rate from 0.0007 s^{-1} to 0.0083 s^{-1} approximately 1 % shift for the material DIN1.4301 as well as for the material DX54D was reached. When changing the strain rate from 0.0007 s^{-1} to 0.0083 s^{-1} , the decrease in elongation of about 3 % for austenitic steel sheet as well as the slight decrease in elongation of about 2 % for drawing quality low carbon steel sheets was also recorded¹.

As it was mentioned FLC reached by experimental measurement and by numerical simulation shows good agreement. Further research should be focused on the analysis of material models in relation to the FLC.

4. Conclusion

New materials bring to vehicles construction new ways to improve their performance – passenger's safety at crash situations, weight loss, etc. Achieved results show the austenitic steel sheets should be included in these materials.

The virtual simulation is commonly used in the design of different variants of design solutions for vehicles and their components as well as in the design of production. In the simulation is necessary to respect the requirements of functionality and manufacturability, which are defined by material properties and used simulation soft-

ware. Functionality requirements are defined by material properties in elastic-plastic area. In crash situations and manufacture of car components by stamping is necessary to supplement this data with data allowing to predict the localization of plastic deformation followed by fracture. Localised plastic deformation for different stress-strain states can be described by FLC. This paper presents a procedure for determining the FLC by video-camera recording and by numerical simulation. Comparing the FLC at different stress-strain states follows that FLC for austenitic steel sheet is situated higher than FLC for low carbon steel sheet. It means austenitic steel sheet shows better formability and ability to absorb impact energy.

This contribution was working out with the support of the grant project VEGA 1/0824/12.

REFERENCES

1. Hrivňák A., Evin E.: *Lisovateľnosť plechov*. Elfa, Košice 2004.
2. Čada R.: *Tvařitelnost ocelových plechu*. Repronis, Ostrava 2001.
3. Rosenberg G., Gaško M., Sinaiova I., Halama M.: *Chem. Listy 105*, s568 (2011).
4. Ramaekers J. A. H.: A Criterion for Local Necking. In.: *6th Shemet*. 2, (1998).
5. Mihalíková M., Ambriško, L., Pešek, L.: *Chem. Listy 104*, s350 (2010).
6. Ganesh Narayanan R., Narasimhan K.: *J. Strain Analysis*. 43, (2008).
7. Kováč P., Tittel V.: *Mater. Sci. Technol.* 5, 5 (2010).
8. Chow L. C., Yang X. J., Chu E.: *J. Eng. Mater. Technol.* 124 (2002).
9. Mishra S. K., et all: *Int. J. Mater. Forming* 2, 59 (2009).

E. Evin, M. Tomáš, and J. Výboch (*Department of Technologies and Materials, Faculty of Mechanical Engineering, Technical University of Kosice*): **Prediction of Local Limit Deformations of Steel Sheets Depending on Deformation Scheme**

Paper presents study results of localised deformation, described by FLC, at different deformation schemes. FLC are used for fracture prediction at crash and formability tests in automotive industry. In experiments were used two types of steel sheets: hot deep galvanized steel sheet DX54D and austenitic stainless steel DIN 1.4301. Limit localised deformations were researched by experimental tests (CCD video camera recording) and numerical simulation. Deformation schemes were modelled on tensile test specimens by different notch radii (R5, R10, R17.5, R25). Reached forming limit curves from experiment and simulation were compared. There was shown good agreement of FLC experimentally measured and computed by numerical simulation.